Multiscale damage modelling of 3D woven composites under static and impact loads

S.Z.H. Shah [a], P.S.M. Megat-Yusoff [a], S. Karuppanan [a], R.S Choudhry [b*], Z Sajid [a]

[a] *Department of Mechanical Engineering, Universiti Teknologi PETRONAS,32610 Bandar Seri Iskandar, Perak, Malaysia*

[b] *College of Science and Engineering, School of Computing and Engineering, Mechanical Engineering Discipline, University of Derby, UK*

**Corresponding author: , Tel: +44 1332 593596, Email: r.choudhry@derby.ac.uk*

Abstract

A multiscale progressive damage modelling methodology for 3-dimensional composites is presented. The proposed methodology is generic and can be implemented in most finite element software to create a digital twin for simulation of damage response. It uses 3D solid element (reduced integration) representation of the part for global analysis, while the local damage response, as well as matrix nonlinearity is modelled using a mesoscale constitutive unit-cell model of 3D woven composite consisting of idealised regions of polymer matrix and impregnated yarns. The idealised unit-cell model is defined based on realistic input from X-ray tomography of the 3D-composite part and the micro-level constituent properties of the matrix and fibres. The damage model has been validated using quasi-static tensile/compression tests as well as dynamic drop-weight impact tests for both thermoset (epoxy) and thermoplastic (Elium) 3D composites. These simulations successfully demonstrate the accuracy and efficiency of the model for both 3D-textile composites.

Keywords: Finite Element Analysis, Damage Modelling, 3D fabric composites, thermoplastic

1. Introduction

The 3D-FRCs are promising materials as compared to 2D-FRCs owing to their superior through-thickness mechanical properties, excellent impact resistance and damage tolerance, due to their inherent safeguard against interlaminar crack propagation [1-5]. In recent years, 3D woven composites have generated much interest within the composite industry, due to their superior transverse properties and ease in the manufacturing provided by near net-shaped designs. Recently, a novel liquid thermoplastic resin system Elium® (a reactive Methyl-methacrylate, MMA) has been introduced by Arkema, which when used with 3D woven composites further improves the impact resistance and damage tolerance of 3D-FRC compared with the conventional thermoset counterpart [6, 7]. These thermoplastic-based 3D woven composites are likely to emerge as a preferred solution to meet the high-volume production demands of the composite industry. In recent publications by the authors [6], it was established that the observed damage mechanisms of the thermoplastic 3D composites are different from both the 2D-laminated and 3D thermoset composites due to their higher ductility and fracture toughness.

The 3D woven FRCs are heterogeneous materials, which comprise of polymer matrix and reinforcement (impregnated yarns) typically arranged in three perpendicular directions. The polymer matrix and reinforcement are contemplated as isotropic and transversely isotropic materials, respectively. However, the composite as a whole exhibits anisotropic properties, due to differences in the reinforcement architecture. The 3D-FRC structures can be subjected to localized damages (particularly impact damage) in the forms of matrix cracking, fibre breakage, debonding and interface failure, which may accrue catastrophic failure under normal operating conditions [4]. Therefore, predicting such damages is a fundamental requirement for the development of safe and reliable composite structures and substantial efforts have been directed towards the development of reliable modelling tools to reduce computational time and physical testing. Multiscale modelling is one of the promising techniques in predicting the mechanical behaviour and damaged response of 3D FRC as it has the potential of being computational efficient while allowing sufficient resolution as well. Not all multiscale models are equally accurate and efficient, and several multiscale models have been reported in the literature to address the influence of complex 3D woven fabric architecture on their damage response, summarized in Table.1.

The multiscale models reported in the literature are broadly divided into three categories, based on the scale-level at which the FE analysis and damage prediction were performed (see Table.1). These multiscale progressive damage models were based on the continuum damage mechanics (CDM) as proposed by Kachanov [8] and Lemaitre and Chaboche [9]. A few authors (category A in Table 1) developed the multiscale progressive damage models, in which a FE based micro model (fibre/matrix unit-cell model) was used to predict the damage response of textile composite at meso-scale or macro-scale. These models were based on a simplified maximum stress criterion and required amplification factors to correlate micro-macro stresses. In comparison, most of the multiscale models available in the literature (category B in Table 1) were based on the meso-scale; where the impregnated yarns and matrix regions were explicitly meshed using finite elements and modelled as a single domain or sub-domain within the global FE model (meso-scale model). The damage was predicted in each constituent to capture fibre failure, yarn debonding and matrix damage. These models have a major drawback of a long computational time, even for small models at the coupon level [10]. Therefore, these multiscale models are not suitable for drop weight impact simulation of FRC, due to their large specimen size. In contrast, a few authors (category C in Table 1) investigated the damage response of 3D composites based on the single orthotropic lamina model (macro-scale model) [11-13], where yarn/matrix regions were not modelled separately. In these models' damage was predicted at macro-scale using different effective stress criteria. These models are computationally efficient; however, they have limited accuracy and they cannot predict failure in individual yarn and matrix regions, due to homogenization assumption. In addition, most of these models were

developed for thermoset composites and do not necessarily capture the unique failure mechanisms observed in thermoplastic composites, described in our previous work [6, 7].

In the case of impact modelling of this novel thermoplastic (Elium) based FRC, Kinvi et al. [14] and Kazemi et al. [15] used a homogenization technique to model the response of 2D woven composite at a macro-scale, where each woven layer was modelled as an orthotropic material. The authors' used maximum stress failure criteria and the nonlinear response was induced using pseudo-plastic law, i.e., by fitting the experimental shear response. However, these models were based on shell elements, which are not suitable for 3D woven composite and impact simulations. To the best of the authors' knowledge, no study has been dedicated to the detailed impact modelling of thermoplastic-based 3D composites and more specifically the novel acrylic-based 3D woven composites. Following these directions, a multiscale progressive model is required for 3D composites, which is both computationally efficient and accurate.

The comparison of the current model with preceding multiscale models is shown in Table 1. It highlights two unique features of the proposed models. Firstly, it combines the benefits of models defined in category B and C. Thus, although the finite element analysis is performed at macro-scale the damage initiation was predicted at meso-scale using analytical meso-scale unit cell model of 3D woven composite Secondly damage evolution in impregnated yarns and matrix regions is modelled separately, using a linear softening law and multilinear law respectively. This approach ensures computational efficiency while providing a high level of accuracy. In the proposed model, each impregnated yarn in the unit-cell is treated as a unidirectional composite and their damage response was predicted through a modified quadratic failure criterion (Hashin failure criteria) [16]. The behaviour of impregnated yarns is assumed as linear elastic until damage initiation, followed by the linear strain-softening law during the damage evolution phase. The linear strain-softening law requires the final failure strain, which is determined through the characteristic length of the impregnated yarn in the unit-cell model. This approach is different from the multiscale progressive damage models reported in the literature (for example category C in Table 1), where the exponential damage evolution function was used. These exponential functions do not require characteristic length; however, they yield rapid damage evolution, which is undesirable for the stability of the FE simulation.

Thus, this work is dedicated to developing a multiscale progressive damage model, within the explicit finite element formulation to predict failure and damage response of 3D FRC. The model is based on continuum damage mechanics, in which the macro-level stress-strain response is evaluated for each time increment using a solid-element based FE mesh. The strains for each element are then updated using a meso-scale analytical unit-cell model of the 3D orthogonal woven composite that predicts failure in individual impregnated yarns and

matrix regions and updates the element stiffness matrix and nodal strains accordingly for the next iteration of the explicit analysis.

The paper is structured as follows. The overall modelling framework is presented in section 2. In section 3 we discuss the specific details of the multiscale progressive damage model component of the framework as applied for 3D woven composites in this study. In Section 4 we discuss the validation of the damage model first by comparing finite element prediction with the tensile response of polymer matrices (ASTM D638) and then by comparing the response of 3D composites under tensile (ASTM D3039) and compressive (ASTM D6641) loading. After the validation of the damage model, it was employed to simulate the drop weight impact test at different impact energies (10 J, 20 J, 30 J, 40 J and 50 J) to predict peak loads, peak deflection and damage patterns, presented in section 5. Finally, to establish the predictive capabilities of the damage model, finite element results have been compared with the inhouse drop weight impact test data, which is discussed in section 6. This work delivers a significant contribution, by developing a multiscale computational framework for 3D woven composites, which offers significant computational efficiency while retaining accuracy. The study demonstrates that the proposed model is successful in virtually investigating the damage response of 3D woven composite made from novel thermoplastic (Elium) and conventional thermoset (epoxy) matrix. Another useful aspect of the work presented in this paper is that the model is validated for both thermoset and thermoplastic 3D-composites which makes the model more widely applicable.

2. Modelling framework

2.1. Continuum damage mechanics and damage modelling

According to the continuum damage mechanics, the load-bearing capability of damaged material is decreased due to the presence of microcracks. These microcracks reduce the load-bearing area A^0 to A^D, which results in high stresses in the intact area. This phenomenon leads to the concept of effective stress, which is the stress acting on the intact area. The effective stresses are related to the nominal stresses using Eqn. (1).

$$\hat{\sigma} = \frac{1}{(1-D)}\sigma \tag{1}$$

where D is a damage variable, which defines the ratio between the original area A^0 and damaged area A^D, given by Eqn. (2).

$$D = \frac{A^D}{A^0} \tag{2}$$

For the three-dimensional stress state, the effective stress in terms of nominal stresses are given by the following relationship [17, 18], see Eqn. (3).

$$\hat{\boldsymbol{\sigma}} = \boldsymbol{D}:\boldsymbol{\sigma} \tag{3}$$
$$\boldsymbol{D} = \boldsymbol{M}^{-1}$$

where, matrix $\boldsymbol{M}$ denotes damage factor matrix, given by Eqn. (4)

$$\boldsymbol{M} = \begin{bmatrix} (1-D_{11}) & & & & & \\ & (1-D_{22}) & & & 0 & \\ & & (1-D_{33}) & & & \\ & & & (1-D_{44}) & & \\ & \text{sym.} & & & (1-D_{55}) & \\ & & & & & (1-D_{66}) \end{bmatrix} \tag{4}$$

Once the material is damaged, the stresses are updated based on the damaged stiffness matrix, see by Eqn. (5)

$$\boldsymbol{\sigma} = \boldsymbol{C}:\boldsymbol{M}:\boldsymbol{\varepsilon} \tag{5}$$
$$\boldsymbol{\sigma} = \boldsymbol{C}^{D}:\boldsymbol{\varepsilon}$$

where, $\boldsymbol{\sigma}$, $\boldsymbol{\varepsilon}$ and $\boldsymbol{C}^{D}$ are stress vector, strain vector and a damaged stiffness matrix, respectively. The damaged stiffness matrix is calculated by multiplying the stiffness matrix $\boldsymbol{C}$ with the damage matrix $\boldsymbol{M}$. The stiffness matrix in terms of elastic constants is given by Eqn. (6)

$$\boldsymbol{C} = \begin{bmatrix} \frac{1-\mathrm{V}_{23}\mathrm{V}_{32}}{\mathrm{E}_{22}\mathrm{E}_{33}\Delta} & \frac{\mathrm{V}_{21}+\mathrm{V}_{31}\mathrm{V}_{23}}{\mathrm{E}_{22}\mathrm{E}_{33}\Delta} & \frac{\mathrm{V}_{31}+\mathrm{V}_{21}\mathrm{V}_{32}}{\mathrm{E}_{22}\mathrm{E}_{33}\Delta} & & & \\ \frac{\mathrm{V}_{12}+\mathrm{V}_{13}\mathrm{V}_{32}}{\mathrm{E}_{11}\mathrm{E}_{33}\Delta} & \frac{1-\mathrm{V}_{31}\mathrm{V}_{13}}{\mathrm{E}_{11}\mathrm{E}_{33}\Delta} & \frac{\mathrm{V}_{32}-\mathrm{V}_{31}\mathrm{V}_{12}}{\mathrm{E}_{11}\mathrm{E}_{33}\Delta} & & 0 & \\ \frac{\mathrm{V}_{13}+\mathrm{V}_{12}\mathrm{V}_{23}}{\mathrm{E}_{22}\mathrm{E}_{11}\Delta} & \frac{\mathrm{V}_{23}+\mathrm{V}_{13}\mathrm{V}_{21}}{\mathrm{E}_{22}\mathrm{E}_{11}\Delta} & \frac{1-\mathrm{V}_{12}\mathrm{V}_{21}}{\mathrm{E}_{22}\mathrm{E}_{11}\Delta} & & & \\ & & & \mathrm{G}_{12} & & \\ & \textit{sym.} & & & \mathrm{G}_{23} & \\ & & & & & \mathrm{G}_{13} \end{bmatrix} \tag{6}$$

$$\Delta = \frac{1-\mathrm{v}_{12}\mathrm{v}_{21}-\mathrm{v}_{23}\mathrm{v}_{32}-\mathrm{v}_{31}\mathrm{v}_{13}-2\mathrm{v}_{12}\mathrm{v}_{23}\mathrm{v}_{31}}{\mathrm{E}_{11}\mathrm{E}_{22}\mathrm{E}_{33}}$$

While calculating the above, the Poisson's ratios should also be degraded, in a similar manner after damage initiation to keep elastic tensor $\boldsymbol{C}$ positive definite, according to Eqn. (7). This Poisson's ratios degradation scheme is consistent with the experimentally observed degradation in the Poisson's ratio, which goes along with damage propagation in composites [19].

$$\frac{v_{ij,D}}{E_{ii,D}} = \frac{v_{ij}(1-D_{ii})}{E_{ii}(1-D_{ii})} = \frac{v_{ji}(1-D_{jj})}{E_{jj}(1-D_{jj})} = \frac{v_{ji,D}}{E_{jj,D}}, i,j = 1,2,3 \tag{7}$$

The irreversibility of the damage variables is defined based on the analysis time *t*, according to Eqn. (8).

$$D_{ii}(t+\Delta t) = Max\{D_{ii}(t), D_{ii}(t+\Delta t)\} \qquad i = 1,2,3 \tag{8}$$

3. Multiscale modelling of 3D composites

The overall flow chart of the proposed multiscale progressive damage model is given in Fig 1. The program uses an explicit dynamic scheme where explicit time marching is used to evaluate each new model state. The overall model consists of three main parts, i.e., a) an analytical micro-mechanics based model to determine elastic constants and strength parameters of impregnated yarns based on properties of dry fabric, resin and relevant volume fractions, b) a macro-scale finite element model of 3D woven composites to determine macro stresses and strains on the component being virtually tested, c) a mathematical meso-scale (unit-cell) model that computes the damaged state and updates the macro model for the next load/displacement increment.

This meso-model is at the heart of the overall model and on one hand, takes the yarn properties and matrix properties as input from the micro-model and on the other hand take the macro-level strains as input from the macro model. Using these values and after applying the appropriate transformations to evaluate stresses in each constituent of the meso-model, the damage response of impregnated yarns and the polymer matrix is predicted using relevant failure criteria. Based on this damage state the element stiffness matrix of the macro model is updated to allow for the correct determination of damage evolution. The process continues in a cycle until a final failure state is achieved. Details of each of these sub-models are presented in the following sub-sections.

3.1. Analytical Micro-scale Model

The impregnated warp, fill, and z-binder yarns are treated as transversely isotropic material, which requires five independent elastic constants to define their elastic response. These elastic constants can be obtained through a micro-scale FE analysis or Chamis model [20]. In this work, Chamis model was used to determine the elastic constants of impregnated yarns, which is given by Eqn. (9).

$$\begin{cases} E_{11} = V_f E_{11,f} + (1 - V_f) E_m \\ E_{22} = E_{33} = \dfrac{E_m}{1 - \sqrt{V_f}(1 - \frac{E_m}{E_{22,f}})} \\ G_{12} = G_{13} = \dfrac{G_m}{1 - \sqrt{V_f}(1 - \frac{G_m}{G_{12,f}})} \\ G_{23} = \dfrac{G_m}{1 - \sqrt{V_f}(1 - \frac{G_m}{G_{23,f}})} \\ v_{12} = V_f v_f + (1 - V_f) v_m \\ v_{23} = \dfrac{E_{22}}{2G_{23}} - 1 \end{cases} \tag{9}$$

where, "V_f"," v_f" "E_f" and "G_f" represent the fibre volume fraction, Poisson's ratio, modulus of elasticity, and modulus of rigidity of the fibres. The constants " v_m" "E_m" and "G_m" represent the Poisson's ratio, modulus of elasticity and modulus of rigidity of the matrix and the constants "E_{11}", "E_{22}", "E_{33}", "G_{12}", "G_{13}", "G_{23}", "v_{12}", "v_{23}" represents the effective modulus of elasticity, modulus of rigidity, and Poisson's ratio of the impregnated yarn in a local coordinate system (LCS). The strength properties of impregnated yarns depend on the fibre volume fraction and strength of individual constituents, i.e., fibre and matrix. For each impregnated yarn the strength was estimated using Chamis model [20] given by Eqn. (10).

$$\begin{cases} X_{11}^T = V_f X_f^T \\ X_{11}^C = V_f X_f^C \\ X_{22}^T = \left[1 - (\sqrt{V_f} - V_f) - \dfrac{E_m}{E_{22,f}}\right] T_m \\ X_{22}^C = \left[1 - (\sqrt{V_f} - V_f) - \dfrac{E_m}{E_{22,f}}\right] C_m \\ S_{12} = \left[1 - (\sqrt{V_f} - V_f) - \left(1 - \dfrac{G_m}{G_{12,f}}\right)\right] S_m \end{cases} \tag{10}$$

where, X_{11}^T, X_{11}^C, X_{22}^T, X_{22}^C and S_{12} represents longitudinal tensile strength, longitudinal compressive strength, transverse tensile strength, transverse compressive strength and in-plane shear strength, respectively of the

impregnated yarn in LCS. X_f^T and X_f^C denote tensile and compressive strength of the fibre. T_m, C_m and S_m denote tensile, compressive and shear strength of the matrix.

3.2 Constitutive Meso-scale Unit-cell Model

In the multiscale modelling, macro-scale behaviour of 3D woven composites is associated with a meso-scale idealised constitutive unit-cell model. This constitutive model plays a crucial role in defining both the elastic and damage evolution behaviour of the 3D composite and is called by the macro-level explicit FE solver at each material integration point to update the model state. The overall algorithm for this interaction between the models at different levels is explained in section 3.5. Here, in this section, we explain the ideal constitutive unit-cell model of the 3D orthogonal woven composites used in this work.

Fig 2(a) shows a schematic representation of this idealized unit-cell model consisting of three impregnated yarns (warp, fill and z-binder) and polymer matrix regions. In this work, it is assumed that in the ideal unit-cell model; a) impregnated yarns (warp, weft and z-binder) are perpendicular to each other, b) the cross-sectional area of each impregnated yarn is rectangular and constant throughout the length, c) there is no waviness in the impregnated yarn, d) there are no voids in the unit-cell model and e) fibre-matrix interface is not explicitly modelled. The idealised unit-cell model is made representative of the actual internal architecture of the 3D woven composite by accounting for correct volumetric proportions of each type of impregnated yarn (warp, weft and z-binder) and the matrix region. This is done by estimating the geometric parameters a_i, b_i and c_i from several cross-sectional X-ray CT-scan images of the actual cured samples. Typical examples of cross-sectional X-ray CT views used in this study are shown in Fig 2(b) to (e). These figures show the top view, warp yarn cross-section, fill cross-section and z-binder yarn cross-section of thermoplastic 3D woven composite, respectively.

In the idealized meso-scale unit-cell model discussed above, yarn waviness and fibre-matrix interface were not modelled, which may accrue some inaccuracies in the predicted response. For example, the 3D fabric architecture used has small yarns waviness, as shown in Fig 2. Adding yarn waviness in the multiscale model may improve the accuracy, however, it will increase the computational cost. The fibre-matrix interface is not included in the model to account for yarn debonding and delamination. This assumption will not make a significant difference in the results, due to two reasons, a) the presence of through-thickness reinforcement in 3D fabric architecture significantly reduces interface debonding and delaminations; therefore, the extent of delamination is only localized, and b) nonlinear response of polymer matrix is separately modelled, thus, to some extent it indirectly considers debonding and localized delamination effects.

3.2.1. Constitutive behaviour of yarns

The 3D orthogonal woven composites consist of three perpendicular impregnated yarns (warp, fill and z-binder), which contains both fibres and matrix. Therefore, these impregnated yarns were treated locally as a transversely isotropic material (unidirectional composites) and analytically modelled according to their orientation and volume fraction in a unit cell. Fig. 3(a) shows the unit-cell model of 3D orthogonal woven composites in the global coordinate system (XYZ). Meanwhile, Fig. 3(b)-(d) shows impregnated warp, weft and z-binder yarn in the local coordinate system (123), respectively. Figure (Fig. 3(b)-(d)) also shows the relationship between the global and local coordinate system of each impregnated yarn. The constitutive modelling of impregnated yarns was first defined in the local (***L***) coordinate system (123) and then transformed into the global (***G***) coordinate system (XYZ), using Eqn. (11).

$$\boldsymbol{\sigma}^G = \left[T_{k/l}^{G|L}\right]^T \boldsymbol{\sigma}^L \tag{11}$$

$$\boldsymbol{\varepsilon}^G = \left[T_{k/l}^{G|L}\right]^T \boldsymbol{\varepsilon}^L$$

$$\boldsymbol{C}^G = \left[T_{k/l}^{G|L}\right]^{-1} [\boldsymbol{C}^L] \left[T_{k/l}^{G|L}\right]^{-T}$$

where, $\boldsymbol{\sigma}^L$, $\boldsymbol{\varepsilon}^L$ and $\boldsymbol{C}^L$ represents the stress vector, strain vector and stiffness matrix in the local coordinate system. $\boldsymbol{\sigma}^G$, $\boldsymbol{\varepsilon}^G$ and $\boldsymbol{C}^G$ represents the stress vector, strain vector and stiffness matrix in the global coordinate system. $T_{k/l}^{G|L}$ denotes the matrix transformation from local to the global coordinate system. The subscript *k* denotes impregnated warp yarn (WY) and fill yarn (FY), and subscript *l* represents impregnated z-yarn (ZY). In the case of 3D orthogonal woven composite, the local and global coordinate system for impregnated warp yarn is the same. The transformation matrix for the impregnated warp and fill yarn is given below, see Eqn. (12).

$$\left[T_k^{G|L}\right] = \begin{bmatrix} cos^2\theta & sin^2\theta & 0 & 0 & 0 & 2cos\theta sin\theta \\ sin^2\theta & cos^2\theta & 0 & 0 & 0 & -2cos\theta sin\theta \\ 0 & 0 & 1 & 0 & 0 & 0 \\ 0 & 0 & 0 & cos\theta & -sin\theta & 0 \\ 0 & 0 & 0 & sin\theta & cos\theta & 0 \\ -cos\theta sin\theta & cos\theta sin\theta & 0 & 0 & 0 & cos^2\theta - sin^2\theta \end{bmatrix} \quad k = WY, FY \tag{12}$$

where, theta θ is the angle of warp and fill impregnated yarns, between global and local coordinate system, which is 0° and 90° counter-clockwise, respectively. The transformation matrix for impregnated z-binder yarn is given by Eqn. (13)

$$\left[T_l^{G|L}\right] = \begin{bmatrix} cos^2\varphi & 0 & sin^2\varphi & 0 & 2cos\varphi sin\varphi & 0 \\ 0 & 1 & 0 & 0 & 0 & 0 \\ sin^2\varphi & 0 & cos^2\varphi & 0 & -2cos\varphi sin\varphi & 0 \\ 0 & 0 & 0 & cos\varphi & 0 & -sin\varphi \\ -cos\varphi sin\varphi & 0 & cos\varphi sin\varphi & 0 & cos^2\varphi - sin^2\varphi & 0 \\ 0 & 0 & 0 & sin\varphi & 0 & cos\varphi \end{bmatrix} \quad l = ZY \tag{13}$$

where, angle φ is the angle of impregnated z-yarn angle, between global and local coordinate systems, which in this case is -90° (clockwise).

Damage initiation criteria for impregnated yarn

The impregnated yarns were modelled as transversely isotropic linear elastic composite up to damage initiation, followed by the linear damage evolution. In this work, modified three-dimensional quadratic failure criteria (Hashin 3D failure criteria) was used to predict damage initiation in each impregnated yarn [16]. It consists of six damage initiation indices to predict fibre failure under longitudinal tensile/compression, matrix failure under in-plane transverse tensile/compression and matrix failure under out-of-plane transverse tensile/compression. Two additional damage modes were considered to predict damage along the out-of-plane transverse direction (or direction 3 in a local coordinate system). The forms of these indices are similar to the in-plane transverse direction. The six damage initiation functions considered in this work are given by Eqn. (14)-(19).

$$F_{1,T} = \left(\frac{\langle \hat{\sigma}_{11} \rangle}{X^T}\right)^2 + \frac{\hat{\tau}_{12}^2}{S_{12}^2} + \frac{\hat{\tau}_{31}^2}{S_{31}^2} \tag{14}$$

$$F_{1,C} = \left(\frac{-\hat{\sigma}_{11}}{X^C}\right)^2 \tag{15}$$

$$F_{2,T} = \left(\frac{\langle \hat{\sigma}_{22} \rangle}{Y^T}\right)^2 + \left(\frac{\hat{\tau}_{12}}{S_{12}}\right)^2 + \left(\frac{\hat{\tau}_{23}}{S_{23}}\right)^2 \tag{16}$$

$$F_{2,C} = \left(\frac{\langle -\hat{\sigma}_{22} \rangle}{2S_{23}}\right)^2 + \left[\left(\frac{Y_C}{2S_{23}}\right)^2 - 1\right]\frac{\hat{\sigma}_{22}}{Y_C} + \left(\frac{\hat{\tau}_{12}}{S_{12}}\right)^2 \tag{17}$$

$$F_{3,T} = \left(\frac{\langle \hat{\sigma}_{33} \rangle}{Z^T}\right)^2 + \left(\frac{\hat{\tau}_{31}}{S_{31}}\right)^2 + \left(\frac{\hat{\tau}_{23}}{S_{23}}\right)^2 \tag{18}$$

$$F_{3,C} = \left(\frac{\langle -\hat{\sigma}_{33} \rangle}{2S_{23}}\right)^2 + \left[\left(\frac{Z_C}{2S_{23}}\right)^2 - 1\right]\frac{\hat{\sigma}_{33}}{Z_C} + \left(\frac{\hat{\tau}_{31}}{S_{31}}\right)^2 \tag{19}$$

where, $F_{1,T}$ and $F_{1,C}$ denote fibre failure under tension and compression; $F_{2,T}$ and $F_{2,C}$ denote matrix in-plane transverse tension and compression failure; $F_{3,T}$ and $F_{3,C}$ denotes matrix out-of-plane transverse tension and compression failure. X^T, Y^T and Z^T represent longitudinal, in-plane transverse and out-of-plane transverse tensile strength, respectively. X^C, Y^C and Z^C represent longitudinal, in-plane transverse and out-of-plane transverse compressive strength, respectively. S_{12}, S_{13} and S_{23} are shear strength in respective planes. All the strength values used above are for equivalent unidirectional composite with same volume fraction as assumed in the unit cell of the impregnated yarn sub-cell being modelled, i.e. warp, fill or z-binder.

Damage evolution criteria for impregnated yarns

Once the damage initiation index exceeded the value of one for any damage mode in a yarn, the corresponding stiffnesses were degraded according to the linear damage evolution law. Thus, the behaviour of each impregnated yarn was considered as bilinear. The strain-based linear softening evolution law used is, given by Eqn. (20).

$$d_{i,\frac{T}{C}} = \left(\frac{\varepsilon_{i,\frac{T}{C}}^{max}}{\varepsilon_{i,\frac{T}{C}}^{max} - \varepsilon_{i,\frac{T}{C}}^{ini}}\right)\left(\frac{\varepsilon_{i,\frac{T}{C}} - \varepsilon_{i,\frac{T}{C}}^{ini}}{\varepsilon_{i,\frac{T}{C}}}\right) \tag{20}$$

where, $\varepsilon_{i,\frac{T}{C}}^{ini}$, $\varepsilon_{i,\frac{T}{C}}$ and $\varepsilon_{i,\frac{T}{C}}^{max}$ represent the strain at damage initiation, current (driving) strain and fully damage strain, respectively. The subscript *i* can take the values 1, 2 or 3 and represents the longitudinal (*i* = 1), in-plane transverse (*i* = 2) and out-of-plane transverse direction (*i* = 3). *T* and *C* denote tension and compression, respectively. The schematic diagram of a linear damage evolution is shown in Fig. 4(a). The linear damage evolution law is defined in Eqn. 20 prescribed the evolution of damage variables with their respective driving strains $\varepsilon_{i,\frac{T}{C}}$ and $d_{i,\frac{T}{C}}$ varies from zero at damage initiation $\left(\varepsilon_{i,\frac{T}{C}} = \varepsilon_{i,\frac{T}{C}}^{ini}\right)$ to one for final failure $\left(\varepsilon_{i,\frac{T}{C}} = \varepsilon_{i,\frac{T}{C}}^{max}\right)$. The strain at failure initiation is not known in advance, as it is recorded by the subroutine for each damage mode once the respective threshold is reached (using Equation 12 to 17). Whereas, the strain at final failure (strain at which the fracture across the element occurs) is determined for each damage mode of the impregnated yarn, using their respective characteristic length $L_{c,i}$ in the unit-cell model, the energy release rate of the damage mode $G_{f,i}$ and ultimate strength of the damage mode $\sigma_{i,\frac{T}{C}}^{ini}$, given by Eqn. (21) [21].

$$\varepsilon_{i,\frac{T}{C}}^{max} = \frac{2\,G_{f,i}}{\sigma_{i,\frac{T}{C}}^{ini}\,L_{c,i}} \tag{21}$$

The characteristic length for each damage mode of the impregnated yarn was determined using their respective dimensions and orientation in the unit-cell (shown in Fig. 2(a)), in the local coordinate system. It is assumed that the size of each element is equal to the size of UC of 3D-FRC, consisting of impregnated yarns (warp, fill and z-binder) and matrix region. The characteristic lengths of constituents were selected for each damage mode, according to their orientation in the UC model, is given in Table 2. The variables (a_i, b_i, c_i) defining the characteristic length of each impregnated yarn are shown in Fig. 2(a). Once the damage is initiated in impregnated yarns, the respective stiffness is reduced according to Eqn. (22).

$$\boldsymbol{C}^{D,f} = \boldsymbol{C}^{f}\,\boldsymbol{M}^{f} \tag{22}$$

$$\boldsymbol{M}^{f} = \begin{bmatrix} \left(1-D_{11}^{f}\right) & & & & & & \\ & \left(1-D_{22}^{f}\right) & & & 0 & & \\ & & \left(1-D_{33}^{f}\right) & & & & \\ & & & \left(1-D_{44}^{f}\right) & & & \\ & & & & \left(1-D_{55}^{f}\right) & & \\ & & sym. & & & & \left(1-D_{66}^{f}\right) \end{bmatrix}$$

where, $\boldsymbol{C}^{D,f}$, $\boldsymbol{C}^{f}$ and $\boldsymbol{M}^{f}$ represent the damage stiffness matrix, undamaged stiffness matrix and damage factor matrix of impregnated yarns. The superscripts "f" represents impregnated yarns. It is worth noticing that more

than one damage mode may also occur in an impregnated yarn during multiaxial loading conditions; therefore, six combined damage variables were defined, which are given by Eqn (23)-(28).

$$D_{11}^f = 1 - (1 - d_{1,T})(1 - d_{1,C}) \tag{23}$$

$$D_{22}^f = 1 - (1 - d_{2,T})(1 - d_{2,C}) \tag{24}$$

$$D_{33}^f = 1 - \left(1 - d_{3,T}\right)\left(1 - d_{3,C}\right) \tag{25}$$

$$D_{44}^f = 1 - (1 - D_{f,11})(1 - D_{f,22}) \tag{26}$$

$$D_{55}^f = 1 - (1 - D_{f,22})(1 - D_{f,33}) \tag{27}$$

$$D_{66}^f = 1 - (1 - D_{f,33})(1 - D_{f,11}) \tag{28}$$

where the damage variables D_{11}^f, D_{22}^f and D_{33}^f, represent normal damage modes (in the fibre direction in a yarn); D_{44}^f and D_{66}^f represent the combination of fibre fracture and matrix transverse (out-of-plane) failure and D_{55}^f denotes matrix transverse (in-plane and out-of-plane) failure. It is postulated that the damage variables D_{44}^f, D_{55}^f and D_{66}^f are not independent and can be expressed as a combination of in-plane damage variables D_{11}^f, D_{22}^f and D_{33}^f [16]. The micro-stresses $\boldsymbol{\sigma}^f$ in individual yarns were updated based on the damage stiffness matrix and global strains $\boldsymbol{\varepsilon}$, given by Eqn. (29)

$$\boldsymbol{\sigma}^f = \boldsymbol{C}^{D,f}\boldsymbol{\varepsilon} \tag{29}$$

3.2.2 Constitutive behaviour of polymer matrix

The behaviour of the pure polymer matrix is considered to be linear elastic prior to failure initiation, followed by the elastoplastic deformation due to damage growth. The elastic tensor of isotropic material $\boldsymbol{C}$ is a function of elastic modulus E_m and Poisson's ratio v_m, given by Eqn. (30).

$$\boldsymbol{\sigma} = \boldsymbol{C}\,\boldsymbol{\varepsilon} \tag{30}$$

Matrix failure initiation criteria

The polymer matrix is considered isotropic in terms of its stiffness however, the tensile and compressive yield strength of the polymer matrix may be different due to the dependency of yielding on the hydrostatic components of the applied stress state. Therefore, a modified von Mises failure criteria in terms of compressive and tensile strength is used [22], given by Eqn. (31).

$$\frac{\sigma_v^2}{C_m T_m} + \left(\frac{1}{T_m} - \frac{1}{C_m}\right) I_1 = 1 \tag{31}$$

where, C_m and T_m represent the compressive and tensile strength of the polymer matrix; σ_v and I_1 represent von Mises stress and first stress invariant, which can be calculated from stress components σ_{ij}^m, given by Eqn. (32)

$$\sigma_v = \sqrt{\frac{1}{2}[(\sigma_{11}^m - \sigma_{22}^m)^2 + (\sigma_{22}^m - \sigma_{33}^m)^2 + (\sigma_{33}^m - \sigma_{11}^m)^2 + 6(\sigma_{12}^{m\,2} + \sigma_{23}^{m\,2} + \sigma_{31}^{m\,2})]} \tag{32}$$

$$I_1 = \sigma_{11}^m + \sigma_{22}^m + \sigma_{33}^m$$

Eqn. 32 can be written in terms of equivalent stress σ_{eq}, see Eqn. (33).

$$\sigma_{eq} = \frac{(\beta-1)I_1 + \sqrt{((\beta-1)I_1)^2 + 4\beta\sigma_v^2}}{2\beta} \tag{33}$$

where β represents the ratio between compressive strength and tensile of the polymer matrix, i.e. $\beta = C_m/T_m$. The equivalent stress can be represented in terms of equivalent strain ε_{eq}, given by Eqn. (34).

$$\varepsilon_{eq} = \frac{(\beta-1)J_1 + \sqrt{((\beta-1)J_1)^2 + (\frac{2-4v^m}{1+v^m})\beta\sigma_v^2}}{2\beta(1-2v^m)} \tag{34}$$

where, v^m and J_1 represent Poisson's ratio and first strain invariant.

Matrix damage evolution

The matrix behaviour prior to failure initiation (elastic limit) is governed by the linear elastic law. Once the failure is initiated the polymer matrix undergoes hardening during damage evolution. The matrix damage evolution used in this work is based on the multi-linear damage evolution law proposed by Xu et al. [23], as shown in Fig. 4(b). The damage evolution d_m^k is calculated based on the yield stress and equivalent strain relationship for each step, given by Eqn. (35).

$$d_m^k = \frac{\sigma_y^{k-1}\left(\varepsilon_y^k - \varepsilon_{eq}\right) + \sigma_y^k\left(\varepsilon_{eq} - \varepsilon_y^{k-1}\right)}{E_{m,0}\varepsilon_{eq}(\varepsilon_y^k - \varepsilon_y^{k-1})} \tag{35}$$

where, ε_y^k and ε_y^{k-1} represent yield strain at damage stage *k* and *k-1*. σ_y^k and σ_y^{k-1} represent yield stress at the damage stage *k* and *k-1*. ε_{eq} is the equivalent strain in *k*th damage stage ($\varepsilon_y^{k-1} < \varepsilon_{eq} \leq \varepsilon_y^k$). $E_{m,0}$ is the undamaged stiffness of a polymer matrix. The final matrix damageD^m at each integration, a point is evaluated for each step, based on the maximum matrix damage calculated for that step based on the Eqn. (36).

$$D^m = Max(1 - d_m^k) \tag{36}$$

Once the maximum damage is achieved in the pure matrix region of the unit-cell, then the stiffness of the matrix region is reduced according to the matrix damage variable given by Eqn (37).

$$\boldsymbol{C}^{D,m} = \boldsymbol{C}^m\,\boldsymbol{M}^m \tag{37}$$

$$\boldsymbol{M}^m = (1 - D^m)\begin{bmatrix} 1 & & & & & \\ & 1 & & & 0 & \\ & & 1 & & & \\ & & & 1 & & \\ & sym. & & & 1 & \\ & & & & & 1 \end{bmatrix}$$

where, $\boldsymbol{C}^{D,m}$, $\boldsymbol{C}^m$ and $\boldsymbol{M}^m$ represent the damage stiffness matrix, undamaged stiffness matrix and inverse of damage matrix of a pure matrix region in the unit-cell. The superscripts "*m*" represents polymer matrix. The micro-stresses $\boldsymbol{\sigma}^m$ in the polymer, matrix regions are updated based on Eqn. (38)

$$\boldsymbol{\sigma}^m = \boldsymbol{C}^{D,m}\,\boldsymbol{\varepsilon} \tag{38}$$

3.3. Macro-scale modelling

The FE analysis was performed at macro-scale in Abaqus/Explicit software, to determine macro-strains due to applied load. In this work we used the mesh size equal to the size of a unit-cell of 3D orthogonal woven composites; therefore each integration point in the macro-scale model represents one unit-cell. The homogenized macro stresses at each integration point were determined using a volume averaging method. According to the volume averaging approach, it is assumed that the homogenized macro stresses in the GCS of the element are evaluated by adding the contributions of individual constituents according to their volume proportion in the unit cell, using Eqn. (39).

$$\bar{\boldsymbol{\sigma}} = \boldsymbol{\sigma}^{m} V^{m} + \boldsymbol{\sigma}^{warp} V^{warp} + \boldsymbol{\sigma}^{fill} V^{fill} + \boldsymbol{\sigma}^{z-binder} V^{z-binder} \quad (39)$$

where $\bar{\boldsymbol{\sigma}}$ represents the macro stresses in the global coordinate system; $\boldsymbol{\sigma}^{m}$ represents the micro stresses in the matrix region; $\boldsymbol{\sigma}^{warp}$, $\boldsymbol{\sigma}^{fill}$ and $\boldsymbol{\sigma}^{z-binder}$ represents the micro stresses in the impregnated warp, fill and z-binder yarn, respectively, in the GCS of the unit cell. V^{m}, V^{warp}, V^{fill} and $V^{z-binder}$ are the corresponding volume fraction of pure matrix, warp yarn, fill yarn and z-binder phases, respectively in the idealised unit-cell and estimated on the basis of cross-sectional X-ray CT-scans as explained earlier in section 3.2.

3.4. Damage variable thresholds

In the progressive damage model, the final component is the definition of the threshold value of damage variables $d_{i,max}$ for each impregnated yarns in the unit-cell (warp, weft and z-yarn) and $d_{m,max}$ for matrix. This threshold value represents the maximum degradation of the engineering stiffness of impregnated yarn and must be specified for each damage mode, to avoid numerical instability which can arise due to excessive element distortion. Based on the degradation factors reported in the literature by Camanho and Matthews [24] and Warren et al. [25], the maximum thresholds were defined for each damage mode. The threshold values for tensile and compressive damage mode were considered independently for longitudinal, in-plane transverse and out-of-plane transverse direction; these threshold values are defined in Table. 3. In the case of tensile failure, the stiffness was reduced to the maximum value, as load-carrying capacity is almost zero due to crack opening. However, in compression, some residual stiffness remains and once the failure has occurred the crushed material and debris is still capable of transmitting the load, as reported by Iannucci and Willows [26]. The threshold values for the shear damage modes are the combination of longitudinal and transverse damage modes thresholds; therefore, the damage threshold depends on the material degradation factor for each. With the definition of a unit-cell model, damage initiation criterion for impregnated yarns and matrix, damage evolution laws for impregnated yarns and matrix, and degradation factors, the multiscale progressive damage model was completed. The following section discusses the numerical implementation of the proposed multiscale damage model, its validation and implementation to a dynamic drop weight impact simulation.

3.5. Numerical implementation of a damage model

The overall algorithm of the multiscale progressive damage model is shown in Fig. 5. The inputs in the damage model are elastic constants of fibres and matrix, strength parameters of fibres and matrix and the parameters defining the unit-cell model of 3D woven composites (UC parameters and volume proportions). The analytical micro-model to predict the effective properties of impregnated yarns (section 3.1), and the constitutive unit-cell model to determine the macro-scale response of 3D composites (section 3.2), was defined in a user-defined subroutine (VUMAT). The finite element simulation was performed at macro-scale in Abaqus/Explicit. At the start of the simulation, VUMAT generates elastic stiffness matrix of each constituent, i.e., $\boldsymbol{C}^{warp,t}$, $\boldsymbol{C}^{fill,t}$, $\boldsymbol{C}^{z-binder,t}$ and $\boldsymbol{C}^{m,t}$, in global coordinate systems (XYZ) of a unit-cell. At each time increment (Δt) the sub-routine receives strain increment ($\Delta\bar{\boldsymbol{\varepsilon}}_n^t$) due to the applied load and state variables for all the damage variables from the previous increment ($t-1$), at integration point (n) of the finite element model. In the first step, VUMAT evaluates the global strains ($\bar{\boldsymbol{\varepsilon}}_n^t$) by adding macro-strains from the previous time increment ($\bar{\boldsymbol{\varepsilon}}_n^{t-1}$) and current strain increment ($\Delta\bar{\boldsymbol{\varepsilon}}_n^t$), at integration point (n) in the global coordinate system. It is assumed that the macro-strains ($\bar{\boldsymbol{\varepsilon}}_n^t$) at the integration point of the macro-scale model and meso-strains ($\boldsymbol{\varepsilon}_n^t$) in each constituent of the unit-cell are identical through an iso-strain assumption ($\bar{\boldsymbol{\varepsilon}}_n^t = \boldsymbol{\varepsilon}_n^t$). In the following step, the meso-stresses ($\boldsymbol{\sigma}_n^{f,t}$, $\boldsymbol{\sigma}_n^{m,t}$) in each constituent were determined using meso-strains ($\boldsymbol{\varepsilon}_n^t$) and stiffness matrix of each constituent in the global coordinate system. These meso-stresses were then transformed with respect to their orientation in the unit-cell to get meso-stresses ($\boldsymbol{\sigma}_n^{f,t}$) of impregnated yarns in the local coordinate system of the unit-cell. Whereas, in the case of the matrix, no transformation was used as the meso-stresses ($\boldsymbol{\sigma}_n^{m,t}$) in the local and global coordinate systems are the same due to their isotropic nature. The meso-stresses in the local coordinate system are used to evaluate the damage initiation function of each constituent, using Eqn. (14)-(19). Once, the damage is initiated the damage variables ($\boldsymbol{D}_n^{f,t}$, $D_n^{m,t}$) were determined using Eqn. (23)-(28) and Eqn. (36). Damage variables at a time (t) were compared with the damage variable at the previous time increment (t-Δt) and updated based on the maximum value, using Eqn. 8. These damage variables are used to update the meso-stresses at the end of time (t) and to evaluate the damage stiffness matrix for the next time increment (t+Δt). The updated meso-stresses in the local coordinate system are transformed back into the global coordinate system, using Eqn. 11. Finally, the homogenized macro-stresses ($\bar{\boldsymbol{\sigma}}_n^t$) at integration point ($n$) were calculated using meso-stresses in the global coordinate system and volume fraction of each constituent in the unit cell (V^i), using Eqn. (39). The same process is repeated for the next integration point (n) and the process continues until the updated macro-stresses are determined for all the integration points in the model. These

macro-stresses are returned to the solver to evaluate strain increment for the next time increment (Δt). The simulation ends, when the total time (t^t) becomes equal to the maximum time set for the simulation.

4. Validation methodology

4.1. Materials and method

In this research work, 3D orthogonal E-glass woven fabric (3D-9871) obtained from TexTech® Industries, USA, was used to manufacture 3D fibre reinforced composites. The fabric consists of three warp layers and four weft layers held together by the z-binder, which travels along the warp direction. The overall thickness of the fabric is 4.3 mm. The fabric consists of 49% fibres along the warp and weft direction and 2% fibres along the thickness direction. The warp and fill count of the fabric is 2.8 EPCM and 1.9 PPCM, respectively. Two different resin systems were used to fabricate 3D-FRC, i.e., thermoplastic resin Elium® 188x0 supplied by Arkema and thermoset resin Epolam® 5015/5015 supplied by Axson [27, 28]. Both types of 3D-FRC were manufactured using vacuum assisted resin infusion process (VARI). The resin Elium® is liquid at room temperature which allows us to fabricate thermoplastic-based 3D-FRC using the VARI process as well. More details on the fabrication process can be found in reference [6]. The average thickness and fibre volume fraction of both types of the 3D composite are 4 mm and 52%, respectively.

4.2. Validation of multiscale progressive damage model

The proposed multiscale progressive damage model has been validated using the quasi-static test on polymer matrix and 3D composite; and dynamic low-velocity impact test on 3D composite.

4.2.1. Quasi-static (tensile) tests on polymer matrix

The tensile response of both polymer matrix available in the literature for Elium® 188 and Elopam® 5015/5015 was used to validate the behaviour of polymer matrix predicted by the model, i.e., tensile coupon test performed by Kazemi et al. [29] on Elium® 188 and Zhang et al. [30] on Epolam® 5015/5015. The tests were performed using a dog-done specimen according to ASTM standard D638. The geometry of the dog-bone specimen along with the dimensions is shown in Fig. 6(a).

4.2.2. Quasi-static (tensile/compression) tests on 3D composites

To validate the tensile/compression response of 3D composites, the uniaxial (tensile and compression) tests were performed on both types of 3D composites along with warp and weft directions. The tensile and compressions tests were performed according to ASTM D3039 [31] and ASTM D6641 [32], respectively. The geometry of the tensile and compression specimen along with the dimensions, boundary and mesh is shown in Fig 6(d) – (f) and Fig. 6(g) – (i), respectively.

4.2.3. Dynamic low-velocity impact tests

The drop weight impact test has been performed at different impact energies (10 J, 20 J, 30 J, 40 J and 50 J, which corresponds to the impact velocity of 1.9 ms^{-1}, 2.7 ms^{-1}, 3.3 ms^{-1}, 3.9 ms^{-1} and 4.4 ms^{-1}) according to ASTM D7136. The tests were conducted on a rectangular specimen 150 mm x 100 mm x 4 mm in dimension, using a 16 mm diameter hemispherical impactor. The mass of the impactor is 5.1 kg. The schematic diagram of the drop weight impact test is shown in Fig. 7(a). More details on the drop weight impact tests can be found in our earlier publication [6]. The summary of the drop weight impact test in terms of damage severity at different impact energies is summarized in Table 4.

4.3. Finite element analysis

4.3.1. Finite element analysis for quasi-static tests on polymer matrix

The validation finite element analysis was carried using the same overall methodology and subroutine as outlined earlier in Fig. 5. This was achieved by setting the volume proportions of the yarn, $V^{warp} = V^{fill} = V^{z-binder} = 0$ and $V^{m} = 1$, and thus effectively deactivating the part related to the 3D-fabric yarns and only activating the matrix related parts of the code. The dog-bone specimen along with the boundary conditions (according to ASTM D638), as shown in Fig. 6(b), was used for the FE simulation of tensile behaviour of both polymer matrices. The specimen was meshed with reduced integration of 3D solid elements (C3D8R), as shown in Fig. 6(c). The elastic constants and strength properties of thermoplastic and thermoset matrix are given in Table. 5. The predicted tensile response in terms of the stress/strain curve was compared with the experimental stress/strain curves reported in the literature for both the matrices [29, 30].

4.3.2. Finite element model for quasi-static tests on 3D composite

In the second case of validation, the multiscale progressive damage model was used to predict the tensile and compressive response of both 3D composites. The tensile and compressive coupon simulation boundary and loading conditions were specified such that the test condition of ASTM standard D3039 [31] and D6641 [32], respectively are reproduced. The geometry along with the boundary conditions used in the finite element analysis of the tensile and compression coupon is shown in Fig 6(e) and Fig. 6(h), while the finite element mesh is shown in Fig. 6(f) and Fig. 6(i), respectively. The finite element model was meshed with reduced integration of solid elements (C3D8R). The C3D8R is a reduced integration element, which has one integration/Gauss point at the centre. The uniaxial tests were simulated under displacement control. The elastic constants and strengths properties of E-Glass fibre and polymer matrix used as input in the multiscale analysis are given in Table 5. Table 6 shows the critical energy release rate of impregnated yarns under different damage modes in thermoplastic and thermoset 3D composites.

4.3.3. Finite element model for dynamic low-velocity impact tests

The drop weight impact test has been simulated in Abaqus/Explicit according to ASTM D7136 [33]. Due to symmetric geometry, the only quarter model of the rectangular plate (150 mm x 100 mm) was modelled using symmetry boundary conditions. To further reduce the computation time, the gripped region (12.5 mm from each side) of the rectangular plate was also excluded and instead displacement boundary conditions as shown in Fig. 7(b) were applied. The hemispherical projectile with a tup diameter of 16 mm was modelled as an analytical rigid body. A 1.27 kg of a point mass was also attached to the tup to balance the weight.

The simulations were performed at five different impact velocities, i.e., 1.9 ms^{-1}, 2.7 ms^{-1}, 3.3 ms^{-1}, 3.9 ms^{-1} and 4.4 ms^{-1}, which corresponds with the velocity just before impact in the drop weight impact experiments for 10 J, 20 J, 30 J, 40 J and 50 J cases respectively. In the FE simulation, these impact velocity was assigned directly to the centre of mass of indentor as an initial condition and no external force field (such as gravity) was applied. The contact between tup and plate was defined using the penalty method and the co-efficient of friction between them was taken as 0.31. The drop weight impact velocity range used in the work falls under low to medium velocity impact and therefore the strain rate effects, which are important for high-velocity impact can be neglected. Thus, no viscoelastic behaviour was considered in the finite element simulations.

5. Results and discussion

5.1. Mesh convergence study

The model consists of a C3D8R reduced integration element. The element size was selected as (2.1 mm, 2.85 mm, 0.46 mm); this is equal to the actual size of a unit cell of the 3D composite. To ascertain the effect of mesh size on the impact performance, a mesh sensitivity study was performed. Four different levels of mesh size were used, i.e., case-a (mesh size < UC size), case-b (mesh size = UC size), case-c and case-d (mesh size > UC size), as shown in Fig. 8(a). In each case, the LVI simulation was performed at 10 J (1.9 ms^{-1}) and the corresponding force/time and displacement/time response was compared, as shown in Fig. 8(b) and (c). It elucidates that, when the mesh size is less than or equal to the UC size, the force/time and displacement/time response shows good correspondence with the experiments. However, in case-c and case-d when the mesh size is greater than the UC size, the force/time response shows a higher deviation from experiments. For each case, the percentage difference from experiments is shown in Fig. 8(d). It highlights that the case-b shows the most accurate results among all cases.

These graphs indicate that the mesh is reasonably converged for the mesh size equal to the unit-cell size. Although in literature one can find examples [16], where, researchers have used smaller element size than the analytically defined meso scale unit-cell size (in context of a related approach used for 2D composites), we argue that when modelling using this approach it is important to keep the element size the same as the meso

level unit-cell size for a realistic macro-to-meso strain transformation as well as the correct interpretation of volume proportions used for meso-to-macro transformation of the stresses. Having the element size the same as the unit cell automatically gets the correct average elemental strains for the meso level model corresponding to each integration point of the FE mesh. If in a particular case an element size smaller than the UC-size must be chosen for convergence requirements, then averaged values from the elements corresponding to the unit-cell size will be required. Since, the meso-scale unit cell, in this case, is small enough we get a good strain resolution from the global (macro) model for an element size equal to the unit cell size. The multiscale model is implemented using reduced integration procedures, due to the nonlinear behaviour of polymer composite materials and to reduce computational time. Using a full integration procedure may improve the simulation accuracy, due to an increase in the integration points; however, it will significantly increase the computational cost.

5.2. Quasi-static tests on polymer matrix

Fig. 9(a) shows the comparison of tensile stress/strain response predicted by the damage model with the experimentally determined stress/strain curves. The thermoplastic matrix shows higher peak strength (70 MPa) as compared to the thermoset matrix (65 MPa) and this is captured reasonably well by the damage model, within 1.9% and 2.7% deviation, respectively. The tensile stress/strain responses of both matrix after the initial linear regime, exhibit nonlinear behaviour with thermoplastic showing a higher degree of non-linearity and significantly larger final failure strain. The thermoplastic matrix exhibits almost two times higher failure strains due to higher matrix ductility and fracture toughness. This higher strain to failure and ductility of the thermoplastic matrix is beneficial for a composite as it decreases the damage severity by giving extra stability to the 3D composites once they are damaged. Fig 9(b) depicts the location of damage predicted by the FE simulation. The simulation shows that the failure occurred in the narrow gauge section, which is according to the standard ASTM standard D638.

5.3. Quasi-static tests on 3D composites

The uniaxial tensile and compression tests were simulated using the multiscale damage model presented in section 3. The results are summarized in Table 7. In thermoplastic 3D composite, the predicted tensile strength along the warp and weft directions were within 3.9% and 7.3% deviations respectively, of their average experimental value. Whereas, the predicted compressive strengths for the thermoplastic 3D composite along the warp and weft directions were within 16% (within 10% for maximum limit) and 2.1% deviations with their experimental average value, respectively. Overall the predicted tensile/compressive strength of thermoplastic 3D composites shows good agreement with the experimental data. In the case of thermoset 3D composites, the predicted tensile strengths along warp and weft directions were 8.5% higher than the maximum

value recorded in the corresponding experiments. In contrast, the predicted compressive strengths along the warp and weft directions were within 17% of the maximum value recorded in corresponding experiments and within 7.3% of the maximum experimental value. The model overpredicts the compressive strength of thermoset composite, this can be due to a number of reasons, for example, the model does not account for voids; change in the orientation of fibre and failure of fibre/matrix interface.

The comparison of predicted tensile and compressive stress/strain response of thermoplastic composite with experimentally determined stress/strain curves is shown in Fig. 10(a)-(d). In all the cases, the predicted stress/strain response lies inside the experimental variation. Also, the predicted tensile/compressive strength along the warp and fill direction is close to each other due to the similar fibre content in both directions,i.e., 49% fibres along the warp and fill direction. In the case of tensile loaded specimens, the damage model successfully captured the initial linear region followed by the nonlinear region, which starts from ~ 0.75% strain, see Fig. 10(a) and (b). This transition of the linear region into the nonlinear region corresponds to the damage initiation strain, afterwards, the stiffness starts to decrease, which is primarily due to matrix micro damages. Such a nonlinear region in the tensile stress/strain curves has also been reported in the experimental study of thermoset 3D composites by Callus et al. [34] and Warren et al. [35]. However, the prediction of such mechanisms has not been demonstrated for the resin-infused thermoplastic 3D composites. The predicted compressive strength along the fill loaded specimens corresponds well with the experimental variations; however, in the case of warp loaded specimens the model slightly over predicts (see Fig. 10(c)). This may be due to material and manufacturing defects such as voids, resin-rich pockets, yarn waviness etc., which were not considered in the unit cell model.

The comparison of predicted tensile and compressive stress/strain curves of thermoset composites along with the experimental variation in the stress/strain curves is shown in Fig. 10(e)-(h). Similar to the thermoplastic composites, the predicted tensile stress/strain curve shows the linear region followed by the nonlinear response, due to damage initiation as discussed earlier. The damage initiation strain limit of the tensile stress/strain curve is (transition of linear to nonlinear region) ~ 0.45% strain, which corresponds with the experimental limits i.e. ~ 0.5% strain (see Fig. 10(e) and (f)). In the case of the compressive stress/strain curve, the model slightly overpredicted compressive strength (see Fig. 10(g) and (h)). Overall the damage model slightly over predicts the tensile and compressive behaviour of thermoset 3D composites. As before, this may be due to effects of defects (voids, resin-rich pockets, yarn waviness etc.) and the week fibre/matrix interface (observed experimentally), which may contribute to the reduction of tensile/compressive strength as these factors were not considered in the damage model.

Fig. 11 shows the comparison of predicted and experimental damage patterns in the thermoplastic and thermoset 3D composites subjected to tensile and compressive load. The multiscale model successfully captured

the desired damage patterns, i.e., fibre and matrix failure in the gauge section of the specimen. The 3D orthogonal woven fabric used has 98% fibres along the warp (0°) and fill (90°) direction; therefore, major failure is expected to occur upon fibre failure. Also, the predicted damage pattern would be similar along both directions, due to the ideal unit-cell model (yarn waviness and voids were not considered). Fig. 11(a) and (b) show the fibre failure in the thermoplastic and thermoset 3D composite, respectively under compressive load. In both cases, failure occurred near the tabs due to fibre micro-buckling. Fig. 11(c) and (d) show fibre failure in the thermoplastic and thermoset composite, respectively under tensile load. The thermoplastic 3D composites show ductile failure due to nonlinear deformation in the matrix followed by the extensive fibre pull-out (see Fig. 11(c)). In comparison, the thermoset 3D composites show brittle failure due to brittle failure in the thermoset matrix and in fibres (see Fig. 11(d)).

5.4. Dynamic low-velocity test on 3D composites

The damage model successfully reproduced the drop weight impact response of both thermoplastic and thermoset 3D-FRC in the whole range of impact energies, i.e., 10 J to 50 J. In addition to this, the model demonstrated improved performance of thermoplastic 3D composites in terms of lower damage area and higher peak force, in comparison with the thermoset counterpart, as observed experimentally.

5.4.1. Comparison of elastic and damage response in 3D-FRC

The preliminary FE simulation to determine the elastic response of thermoplastic and thermoset 3D composites at 50 J (4.4 ms^{-1}) is shown in Fig. 12. The elastic simulation indicates that in the absence of progressive damage sub-routine the simulation shows significant higher peak force, less displacement and higher rebounding velocity. Thus, the elastic simulation demonstrates the necessity to consider different types of damages mechanisms, observed experimentally in the finite element simulation to accurately predict the damage response of 3D composites under drop weight impact.

5.4.2. Comparison of damage response under LVI (experiment vs. simulation)

Fig. 13 shows the comparison of predicted force/displacement response of thermoplastic and thermoset 3D composites at different impact energies (i.e., 10 J (1.9 ms^{-1}) to 50 J (4.4 ms^{-1}) with the experimentally determined force/ displacement response. As the indentor comes in contact with the specimens, the contact force between them increases linearly, followed by the slight load drop due to micro-damages in the matrix. This was supplanted by the damage propagation process, which completely stopped the indentor at the peak load. The figure indicates that as the impact energy increases from 10 J to 50 J the corresponding maximum displacement and peak force experienced by the specimens increases, as a result, the energy dissipated by the specimen increases. At all impact energies, the finite element simulation demonstrates an excellent correlation of the

material response in terms of damage propagation process, peak load experienced by the specimen and rebounding process of the indentor, which was physically observed in the drop weight impact test (see Fig. 13). After reaching the peak displacement, there is a slight difference between experimental and simulation results, during the rebounding phase. This may be due to a difference in the rebounding velocity of the indentor, as the gravitational effects were ignored during the finite element simulation (see Fig. 13). The area enclosed within the loading and unloading curves represents the amount of energy dissipated by the 3D composite, during the damage process. The dissipated energy evaluated from the FE analysis is slightly less than the experimental dissipated energy.

Fig.14 shows the comparison of predicted velocity-time curves with experiments at different impact velocities. As the tup come in contact with the specimen, the velocity of the tup decreases until it was reduced to zero, where the tup experienced maximum force and peak displacement, as shown in Fig. 13. At this point, both experimental and simulation results show excellent correlation. Afterwards, the rebounding phase starts due to the elastic energy stored in the specimen. In both types of 3D composites, during the rebounding phase, the velocity in simulation is slightly higher than in experiments in all cases. This difference in the predicted and experimental rebound velocity is may be due to the gravitational effect, which was not considered in the finite element simulation.

5.4.3 Comparison of computation time

One of the key benefits of the proposed multiscale progressive damage model is significantly less computational time. This benefit becomes a major concern in the case of large scale dynamic simulations. For example, to perform the dynamic drop weight impact simulation discussed above; the simulation takes around 16 min to complete (4 CPU cores), which is much faster than the former multiscale models (reported in Table 1, category B). For example, the meso-scale model proposed by Turner et al. [36] takes around 8 hours run time (8 CPU cores); whereas, Chu et al. [37] reported 15 hours run time (32 CPU cores) to complete dynamic impact simulation. The more detailed comparison of computational time with other models have been summarized in Table 8.

5.4.4. Comparison of damage severity: Thermoset 3D-FRC vs. thermoplastic 3D-FRC

Fig. 15 shows the comparison of damage predicted by the FE simulation in the thermoplastic and thermoset 3D composites. Overall the thermoset 3D composites show higher damages at all impact energies, which is consistent with the experimental observation. Fig. 15(a) shows the comparison of predicted tensile/compression failure in polymer matrix region in both 3D composites. Several aspects of the damage process in both 3D composites can be understood and compared to this. Firstly, in both cases, the matrix fails due to tensile damage which starts from the bottom (back face) and propagates upward (impact face); whereas,

the matrix compression damage occurs at the top surface (impact face) by the tup. Secondly, the matrix tensile damage is much more pronounced than matrix compressive damage in both cases. In addition, the damage severity increases with the increase in the impact energy. Thirdly, the thermoset matrix experienced higher damage in the thermoset 3D composite as compared to the thermoplastic counterpart. The higher damage in the thermoset composite is due to the brittle nature of the epoxy matrix that undergoes matrix cracking in resin-rich pockets and failed earlier due to its lower strain to failure. In contrast, the thermoplastic matrix undergoes plastic deformation in the resin-rich pockets resulting in reduced damage at all impact energies, due to their higher strains to failure.

Fig. 15(b) shows the combined longitudinal tensile/compressive failure in all three yarns (warp, weft and z-yarn). The tensile failure occurred at the bottom surface and compressive failure occurs at the top surface, due to global deformation in the specimen and compressive failure due to indentor, respectively. Similarly, in this fibre tensile damage at the bottom surface is higher than at the top surface due to fibre compression damage. The thermoset 3D composites exhibit higher damage than thermoplastic composites. However, the fibre failure predicted by the damage model in the thermoplastic 3D composite is slightly higher.

Fig 15(c) shows the comparison of combined in-plane transverse tensile/compressive failure; whereas, Fig. 15(d) shows the comparison of out-of-plane transverse tensile/compressive failure, in the warp and fill impregnated yarn. In this case of the out-of-plane transverse direction, the main failure occurred due to localised crushing under the indentor. However, in both cases, thermoset 3D composite shows higher damage severity, which corresponds to matrix cracking and shear failure. In comparison, the thermoplastic 3D composites show significantly reduce damages, due to plastic deformation. The transverse failure in both composites is governed by the matrix properties, as the thermoset matrix has a brittle behaviour due to its lower strains to failure, which accrue higher damage. In contrast, the thermoplastic matrix has a ductile behaviour and higher strain to failure, which is beneficial in improving the performance of thermoplastic-based 3D composites under drop weight impact loads, as predicted by the damage model.

5.4.5. Comparison of damage area in both 3D-FRC: Experiment vs. Simulation

Fig. 16 shows the comparison of damage area predicted by the FE simulations and through experiments at different impact energies. The predicted damage area shown in Fig. 16 is a cumulative damage area in 3D composites, due to nonlinear deformation of matrix, longitudinal fibre failure, shear failure in the in-plane transverse direction and shear failure in out-of-plane transverse damage. This allows us to get the total extent of the damage which can then be compared with the damaged area measured in experiments (please see detailed experimental results of damage area and calculation method for a damaged area in our previous publication [6]) The red and black dashed line represents damage area determined through experiments in thermoplastic and

thermoset 3D composites, respectively. The predicted and experimental damaged areas were superimposed to make a clear comparison. The proposed multiscale progressive damage model successfully demonstrates the damage severity (footprints) in both 3D composites, at all impact energies. In both 3D composites, the predicted damage area increases with impact energy and the damage severity is much more pronounced in thermoset composite as observed experimentally. This was mainly due to, a) higher matrix damage in thermoset composites in the form of matrix cracking and yarn debonding and b) fibre failure at the bottom surface of the specimens due to tensile damage observed experimentally. These results establish that the impact response and damage severity predicted by the proposed multiscale progressive damage model corroborates well with the experimental results. It also confirms that the resin-infused thermoplastic-based 3D composite reduces the damage severity caused by the impact, thereby enhancing the damage resistance.

6. Conclusion

This work presents a novel multiscale progressive damage model developed to predict the damage response of 3D textile composites. The proposed progressive damage model was implemented in a user-defined subroutine (VUMAT) and simulated in commercially available finite element software, Abaqus/Explicit. The methodology, however, is generic and can be easily used with most dynamic FE solvers that allow for user material definition and reduced integration solid elements. The predictive capability of the damaged model was first demonstrated by simulating the uniaxial test (polymer matrix and 3D-FRC) and then the drop weight impact test of 3D-FRC at different impact energies. A good correlation was achieved between numerical predictions and experimental results. The proposed multiscale progressive damage model successfully captured the uniaxial response of polymer matrix and 3D textile composite in terms of ultimate strength, modulus and failure strain in the case of quasi-static simulations. Whereas dynamic (drop weight impact) simulations accurately predicted the impact response in terms of peak load, maximum displacement and damage severity in both 3D textile composites. The study demonstrates that the proposed multiscale progressive damage model is computationally efficient and successful in virtually investigating the damage response of 3D textile composite made from novel thermoplastic (Elium) and conventional thermoset (epoxy) matrix. The multiscale approach presented here makes it easy to create digital twins for realistic damage simulations because of low computational cost, good accuracy and simple model setup. With the growing interest in using easy to recycle thermoplastic 3D composites and in using digital twins for simulation, the work presented is timely and should benefit a wide audience.

Acknowledgements

The authors would like to acknowledge the financial support provided by Universiti Teknologi PETRONAS (grant number 015LC0-197). The authors would also like to acknowledge the support of Dr. Pierre Gerard from

Arkema and Dr. Sharp Keith from TexTech industries in acquiring Elium® resin and 3D fabric for this research work, Dr. Faiz Ahmad and Advance Functional Material (AFM) lab Universiti Teknologi PETRONAS in providing the facility for the fabrication of 3D composites.

Conflicts of interest

The authors declare no conflict of interest with respect to the research or publication of this work.

References.

[1] Hart KR, Chia PXL, Sheridan LE, Wetzel ED, Sottos NR, White SR. Mechanisms and characterization of impact damage in 2D and 3D woven fiber-reinforced composites. Composites Part A: Applied Science and Manufacturing. 2017;101:432-43.
[2] Saleh MN, El-Dessouky HM, Saeedifar M, De Freitas ST, Scaife RJ, Zarouchas D. Compression after multiple low velocity impacts of NCF, 2D and 3D woven composites. Composites Part A: Applied Science and Manufacturing. 2019;125:105576.
[3] Bandaru AK, Chavan VV, Ahmad S, Alagirusamy R, Bhatnagar N. Low velocity impact response of 2D and 3D Kevlar/polypropylene composites. International Journal of Impact Engineering. 2016;93:136-43.
[4] Shah S, Karuppanan S, Megat-Yusoff P, Sajid Z. Impact resistance and damage tolerance of fiber reinforced composites: A review. Composite Structures. 2019;217:100-21.
[5] Shah S, Choudhry RS, Khan LA. Challenges in compression testing of 3D angle-interlocked woven-glass fabric-reinforced polymeric composites. ASTM Journal of Testing and Evaluation. 2017;5:1502-23.
[6] Shah S, Megat-Yusoff P, Karuppanan S, Choudhry R, Ahmad F, Sajid Z, et al. Performance comparison of resin-infused thermoplastic and thermoset 3D fabric composites under impact loading. International Journal of Mechanical Sciences. 2020;189:105984.
[7] Shah S, Megat-Yusoff P, Karuppanan S, Choudhry R, Ud Din I, Othman A, et al. Compression and buckling after impact response of resin-infused thermoplastic and thermoset 3D woven composites. Composites Part B: Engineering. 2021;207.
[8] Kachanov LM. Time of the rupture process under creep conditions, Izy Akad. Nank SSR Otd Tech Nauk. 1958;8:26-31.
[9] Lemaitre J, Chaboche J-L. Mechanics of solid materials: Cambridge university press, 1994.
[10] Liu G, Zhang L, Guo L, Liao F, Zheng T, Zhong S. Multi-scale progressive failure simulation of 3D woven composites under uniaxial tension. Composite Structures. 2019;208:233-43.
[11] Bandaru AK, Patel S, Sachan Y, Alagirusamy R, Bhatnagar N, Ahmad S. Low velocity impact response of 3D angle-interlock Kevlar/basalt reinforced polypropylene composites. Materials & Design. 2016;105:323-32.
[12] Elias A, Laurin F, Kaminski M, Gornet L. Experimental and numerical investigations of low energy/velocity impact damage generated in 3D woven composite with polymer matrix. Composite Structures. 2017;159:228-39.
[13] Muñoz R, Martínez-Hergueta F, Gálvez F, González C, LLorca J. Ballistic performance of hybrid 3D woven composites: experiments and simulations. Composite Structures. 2015;127:141-51.
[14] Kinvi-Dossou G, Matadi Boumbimba R, Bonfoh N, Koutsawa Y, Eccli D, Gerard P. A numerical homogenization of E-glass/acrylic woven composite laminates: Application to low velocity impact. Composite Structures. 2018;200:540-54.
[15] Kazemi ME, Shanmugam L, Dadashi A, Shakouri M, Lu D, Du Z, et al. Investigating the roles of fiber, resin, and stacking sequence on the low-velocity impact response of novel hybrid thermoplastic composites. Composites Part B: Engineering. 2021;207.
[16] Xu ZW, Chen YH, Cantwell WJ, Guan ZW. Multiscale modelling of scaling effects in the impact response of plain woven composites. Composites Part B: Engineering. 2020;188.
[17] Singh H, Mahajan P. Modeling damage induced plasticity for low velocity impact simulation of three dimensional fiber reinforced composite. Composite Structures. 2015;131:290-303.
[18] Ud Din I, Tu S, Hao P, Panier S, Khan KA, Umer R, et al. Sequential damage study induced in fiber reinforced composites by shear and tensile stress using a newly developed Arcan fixture. Journal of Materials Research and Technology. 2020;9:13352-64.
[19] Tan W, Falzon BG, Chiu LN, Price M. Predicting low velocity impact damage and Compression After Impact (CAI) behaviour of composite laminates. Composites Part A: Applied Science and Manufacturing. 2015;71:212-26.
[20] Chamis CC. Simplified composite micromechanics equations for hygral, thermal and mechanical properties. SAMPE Quarterly. 1984;4:14-33.
[21] Bažant ZP, Oh BH. Crack band theory for fracture of concrete. Matériaux et construction. 1983;16:155-77.
[22] Raghava R, Caddell RM, Yeh GS. The macroscopic yield behaviour of polymers. Journal of Materials Science. 1973;8:225-32.

[23] Xu L, Jin CZ, Ha SK. Ultimate strength prediction of braided textile composites using a multi-scale approach. Journal of Composite Materials. 2014;49:477-94.
[24] Camanho PP, Matthews F. A progressive damage model for mechanically fastened joints in composite laminates. Journal of Composite Materials. 1999;33:2248-80.
[25] Warren KC, Lopez-Anido RA, Vel SS, Bayraktar HH. Progressive failure analysis of three-dimensional woven carbon composites in single-bolt, double-shear bearing. Composites Part B: Engineering. 2016;84:266-76.
[26] Iannucci L, Willows M. An energy based damage mechanics approach to modelling impact onto woven composite materials Part I: Numerical models. Composites Part A: Applied Science and Manufacturing. 2006;37:2041-56.
[27] Sajid Z, Karuppanan S, Kee KE, Sallih N, Shah SZH. Carbon/basalt hybrid composite bolted joint for improved bearing performance and cost efficiency. Composite Structures. 2021;275.
[28] Sajid Z, Karuppanan S, Sallih N, Kee KE, Shah SZH. Role of washer size in mitigating adverse effects of bolt-hole clearance in a single-lap, single-bolt basalt composite joint. Composite Structures. 2021;266.
[29] Kazemi ME, Shanmugam L, Lu D, Wang X, Wang B, Yang J. Mechanical properties and failure modes of hybrid fiber reinforced polymer composites with a novel liquid thermoplastic resin, Elium®. Composites Part A: Applied Science and Manufacturing. 2019;125.
[30] Zhang H, Yang J. Development of self-healing polymers via amine–epoxy chemistry: II. Systematic evaluation of self-healing performance. Smart Materials and Structures. 2014;23.
[31] ASTM. D3039/D3039M-17 Standard Test Method for Tensile Properties of Polymer Matrix Composite Materials. 2017.
[32] ASTM D6641 / D6641M-16e1, Standard Test Method for Compressive Properties of Polymer Matrix Composite Materials Using a Combined Loading Compression (CLC) Test Fixture, ASTM International, West Conshohocken, PA. . 2015.
[33] ASTM D7136 / D7136M-05, Standard Test Method for Measuring the Damage Resistance of a Fiber-Reinforced Polymer Matrix Composite to a Drop-Weight Impact Event, ASTM International, West Conshohocken, PA. 2005.
[34] Callus P, Mouritz A, Bannister MK, Leong K. Tensile properties and failure mechanisms of 3D woven GRP composites. Composites Part A: Applied Science and Manufacturing. 1999;30:1277-87.
[35] Warren KC, Lopez-Anido RA, Goering J. Experimental investigation of three-dimensional woven composites. Composites Part A: Applied Science and Manufacturing. 2015;73:242-59.
[36] Turner P, Liu T, Zeng X, Brown K. Three-dimensional woven carbon fibre polymer composite beams and plates under ballistic impact. Composite Structures. 2018;185:483-95.
[37] Chu T-L, Ha-Minh C, Imad A. Analysis of local and global localizations on the failure phenomenon of 3D interlock woven fabrics under ballistic impact. Composite Structures. 2017;159:267-77.
[38] Wang L, Wu J, Chen C, Zheng C, Li B, Joshi SC, et al. Progressive failure analysis of 2D woven composites at the meso-micro scale. Composite Structures. 2017;178:395-405.
[39] Jia X, Xia Z, Gu B. Numerical analyses of 3D orthogonal woven composite under three-point bending from multi-scale microstructure approach. Computational Materials Science. 2013;79:468-77.
[40] Yang Z, Yan H. Multiscale modeling and failure analysis of an 8-harness satin woven composite. Composite Structures. 2020;242.
[41] He C, Ge J, Qi D, Gao J, Chen Y, Liang J, et al. A multiscale elasto-plastic damage model for the nonlinear behavior of 3D braided composites. Composites Science and Technology. 2019;171:21-33.
[42] Madke RR, Chowdhury R. A multiscale continuum model for inelastic behavior of woven composite. Composite Structures. 2019;226.
[43] Ren C, Liu T, Siddique A, Sun B, Gu B. High-speed visualizing and mesoscale modeling for deformation and damage of 3D angle-interlock woven composites subjected to transverse impacts. International Journal of Mechanical Sciences. 2018;140:119-32.
[44] Ma P, Jin L, Wu L. Experimental and numerical comparisons of ballistic impact behaviors between 3D angle-interlock woven fabric and its reinforced composite. Journal of Industrial Textiles. 2018;48.
[45] El Said B, Daghia F, Ivanov D, Hallett SR. An iterative multiscale modelling approach for nonlinear analysis of 3D composites. International Journal of Solids and Structures. 2018;132-133:42-58.
[46] Turner P, Liu T, Zeng X. Collapse of 3D orthogonal woven carbon fibre composites under in-plane tension/compression and out-of-plane bending. Composite Structures. 2016;142:286-97.
[47] Dai S, Cunningham P. Multi-scale damage modelling of 3D woven composites under uni-axial tension. Composite Structures. 2016;142:298-312.
[48] Zhong S, Guo L, Lu H, Zeng T. A continuum damage model for three-dimensional woven composites and finite element implementation. Composite Structures. 2015;128:1-9.
[49] Zhang C, Li N, Wang W, Binienda WK, Fang H. Progressive damage simulation of triaxially braided composite using a 3D meso-scale finite element model. Composite Structures. 2015;125:104-16.
[50] Green S, Matveev M, Long A, Ivanov D, Hallett S. Mechanical modelling of 3D woven composites considering realistic unit cell geometry. Composite Structures. 2014;118:284-93.
[51] Sun B, Liu Y, Gu B. A unit cell approach of finite element calculation of ballistic impact damage of 3-D orthogonal woven composite. Composites Part B: Engineering. 2009;40:552-60.

[52] Hao A, Sun B, Qiu Y, Gu B. Dynamic properties of 3-D orthogonal woven composite T-beam under transverse impact. Composites Part A: Applied Science and Manufacturing. 2008;39:1073-82.
[53] Liu Y, Straumit I, Vasiukov D, Lomov SV, Panier S. Prediction of linear and non-linear behavior of 3D woven composite using mesoscopic voxel models reconstructed from X-ray micro-tomography. Composite Structures. 2017;179:568-79.

Figures and Captions

Figure 1. Overall flowchart of multi-scale modelling of 3D composites

Figure 2. CT-scan images and unit-cell of 3D woven composite. (a) schematic diagram of the unit-cell model for 3D composites, (b) CT-scan images of the top view, (c) CT-scan image of warp cross-section, (d) CT-scan image of fill cross-section, (e) CT-scan image of z-binder cross-section.

Figure 3. Schematic diagram of a unit-cell model for 3D composites in the global coordinate system (GCS) and the local coordinate system (LCS). (a) unit-cell model of 3D composite in GCS (XYZ), (b) relationship between LCS(123) and GCS(XYZ) of impregnated warp yarn, (c) relationship between LCS(123) and GCS(XYZ) of impregnated fill yarn and (d)) relationship between LCS(123) and GCS(XYZ) of impregnated z-binder yarn.

Figure 4. The schematic diagram of the damage model for impregnated yarns and matrix regions. The superscripts "*f*" and "*m*" represents impregnated yarns and polymer matrix, respectively. (a) bilinear damage evolution law for impregnated yarns and (b) multilinear damage model for polymer matrix.

Figure 5. Overall algorithm for damage prediction in 3D composite using the multiscale method. The superscripts "*f*" and "*m*" represents impregnated yarns and polymer matrix, respectively.

Figure 6. Schematic diagram of geometry and boundary conditions of (a) – (c) dog-bone, (d) – (f) tensile and (g) – (i) compression test simulation. (a), (d), (g) specimen geometry with dimensions; (b), (e), (h) boundary conditions for the FE analysis; (c), (f), (i) shows finite element Mesh of the specimen in each case.

Figure 7. Schematic diagram of a drop-weight impact test setup and FE model. (a) schematic diagram of a drop-weight impact test setup and (b) finite element model used for numerical simulation

Figure 8. Mesh sensitivity study. (a) mesh refinement cases, (b) force/time response, (c) displacement/time, and (d) % difference between experiments and different mesh refinement cases.

Figure 9. Comparison of thermoplastic and thermoset neat matrix under tensile loading. (a) nonlinear behaviour of thermoplastic and thermoset neat matrix under tensile loading and (b) predicted damage in the Dog-bone specimen. The state variable SDV7 represents tensile/compressive failure in the matrix.

Figure 10. Comparison of stress/strain curves of thermoplastic (TP) and thermoset (TS) 3D composites (experimental vs. simulation). (a) TP warp loaded tensile test, (b) TP fill loaded tensile test, (c) TP warp loaded compressive test, (d) TP fill loaded compressive test, (e) TS warp loaded tensile test, (f) TS fill loaded tensile test, (g) TS warp loaded compressive test and (h) TS fill loaded compressive test.

Figure 11. Comparison of damage morphologies in 3D composites (experimental vs. simulation). (a) compressive failure in thermoplastic specimens, (b) compressive failure in thermoset specimens, (c) tensile failure in thermoplastic specimens and (d) tensile failure in thermoset specimens

Figure 12. Comparison of elastic and damage response of thermoplastic and thermoset 3D composites at 50 J. (a) force/displacement response of TP composite, (b) velocity/time response of TP composite, (a) force/displacement response of TS composite and (b) velocity/time response of TS composite

Figure 13. Comparison (experimental vs. simulation results) of the force-time response of 3D thermoplastic composite at different impact energies.

Figure 14. Comparison (experimental vs. simulation results) of the velocity-time response of 3D thermoplastic composite at different impact energies.

Figure 15. Comparison of predicted damage in thermoplastic and thermoset 3D composites at 40 J. (a) matrix failure (represented by SVD25), (b) longitudinal tensile/compressive fibre failure (represented by SVD26), (c) in-plane transverse tensile/compressive matrix failure (represented by SVD27) and (d) out-of-plane transverse tensile/compressive matrix failure (represented by SVD28).

Figure 16. Comparison of damage area (experimental vs. simulation) in thermoplastic and thermoset 3D composites at 10 J, 20 J, 30 J, 40 J and 50 J. The figure shows combined damage due to pure matrix failure, longitudinal damage, in-plane transverse damage and out-of-plane transverse damage. The red and black dashed line represents damage area obtained from experiments in thermoplastic and thermoset 3D composites, respectively. The state variable SDV29 represents combined fibre fracture and matrix failure (in-plane and out-of-plane transverse direction).

Tables

Table 1. Summary of multiscale progressive damage models available in the literature (MiS = Micro-scale, MeS = Meso-scale, MaS = Macro-scale)

Cat.	Reference & year	Fabric architecture	FE mesh - scale-level	Damage initiation in fibre/yarns - scale-level	Damage initiation in matrix	Damage evolution
A	Wang et al. [38] 2017	2D woven	MeS	Max stress (MiS)	Strain invariant criteria	Linear
	Xu et al. [23] 2014	2D braided	MeS	Max stress (MiS)	Strain invariant criteria	None
	Jia et al. [39] 2013	3D orthogonal	MaS	Max stress (MiS)	None	None
B	Yang et al. [40] 2020	2D woven	MeS	Maximum stress (MeS)	Strain invariant criteria	Linear
	Xu et al. [16] 2020	2D woven	MaS	Hashin failure criteria (MeS)	Nonlinear model	Exponential
	He et al. [41] 2019	3D braided	MeS	Hashin failure criteria (MeS)	Parabolic yield criteria	Exponential
	Madke et al. [42] 2019	2D and 3D woven	MeS	Hashin failure criteria (MeS)	None	Linear
	Liu et al. [10] 2019	3D angle-interlock	MeS	Puck failure criteria (MeS)	Parabolic yield criteria	Exponential
	Ren et al. [43] 2018	3D angle-interlock	MeS	Hill failure criteria (MeS)	von Mises yield criteria	Linear
	Pibo et al. [44] 2018	3D angle-interlock	MeS	Maximum stress (MeS)	Maximum stress	None
	Said et al. [45] 2018	3D orthogonal	MeS	Puck failure criteria (MeS)	von Mises criteria	Linear
	Turner et al. [46] 2016	3D orthogonal	MeS	Hashin failure criteria (MeS)	None	Linear
	Warren et al. [25] 2016	3D angle-interlock	MeS	Hashin failure criteria (MeS)	None	Exponential
	Dai et al. [47] 2016	3D orthogonal	MeS	Puck failure criteria (MeS)	Maximum stress criteria	Linear
	Zhong et al. [48] 2015	3D angle-interlock	MeS	Puck failure criteria (MeS)	Parabolic yield criteria	Exponential
	Zhang et al. [49] 2015	2D braided	MeS	Hashin failure criteria (MeS)	None	Linear
	Greens et al. [50] 2014	3D orthogonal	MeS	Maximum stress (MeS)	von Mises yield criteria	None
C	Kazemi et al. [15] 2020	2D woven	MaS	Maximum stress (MaS)	None	None
	Kinvi et al. [14] 2018	2D woven	MaS	Maximum stress (MaS)	None	None
	Bandaru et al. [11] 2016	3D woven	MaS	Chang-Chang model (MaS)	None	None
	Munoz et al. [13] 2015	3D orthogonal	MaS	Maximum stress (MaS)	None	Exponential
	Sun et al. [51] 2009	3D orthogonal	MaS	Critical damage area (MaS)	None	None
	Hao et al. [52] 2008	3D orthogonal	MaS	Critical damage area (MaS)	None	None
B&C	Current model	3D orthogonal	MaS	Hashin failure criteria (MeS)	Strain invariant criteria	Yarns=Linear Matrix=Multilinear

Table 2. Characteristic length for impregnated warp, fill and z-binder yarn for each damage mode.

Damage modes (LCS)	Warp yarn	Fill yarn	Z-binder yarn
Longitudinal tensile/compressive	$L_{c,1} = b_2$	$L_{c,1} = a_2$	$L_{c,1} = a_1$
In-plane transverse tensile/compressive	$L_{c,2} = a_1 + a_2$	$L_{c,2} = b_1 + b_2$	$L_{c,2} = c_1 + c_2$
Out-of-plane transverse tensile/compressive	$L_{c,3} = a_1 + a_2$	$L_{c,3} = b_1 + b_2$	$L_{c,3} = c_1 + c_2$

Table 3. Damage variable thresholds for each damage mode.

Damage modes	Damage variable threshold
Pure matrix regions	$d_{m,max} = 0.98$
Longitudinal damage mode	$d_{1,max} = \begin{cases} 0.95 & tension \\ 0.8 & compression \end{cases}$
The in-plane transverse damage mode	$d_{2,max} = \begin{cases} 0.9 & tension \\ 0.8 & compression \end{cases}$
The out-of-plane transverse damage mode	$d_{3,max} = \begin{cases} 0.9 & tension \\ 0.8 & compression \end{cases}$

Table 4. The relative severity of damage mechanisms for different velocity (single low-velocity impact event)

Material	Damage scale	Damage mechanisms	**Case-1** (10 J/1.9 ms^{-1})	**Case-2** (20 J/2.7 ms^{-1})	**Case-3** (30 J/3.3 ms^{-1})	**Case-4** (40 J/3.9 ms^{-1})	**Case-5** (50 J/4.4 ms^{-1})
3D-TP-FRC	Micro damage	Fibre breakage	None	Some	Some	Moderate	Moderate
		Plasticization	Some	Dominant	Dominant	Significant	Significant
		Matrix cracking	None	None	Some	Moderate	Moderate
	Macro-damage	Yarn debonding	None	Some	Some	Moderate	Moderate
		Z-crown failure	None	None	Some	Moderate	Moderate
		Surface VID	None	BV	CV	CV (>Case 3)	CV (>Case 4)
3D-TS-FRC	Micro damage	Fibre breakage	None	Some	Some	Significant	Significant
		Plasticization	None	None	None	None	None
		Matrix cracking	Some	Dominant	Dominant	Significant	Significant
	Macro-damage	Yarn debonding	Some	Dominant	Dominant	Significant	Significant
		Z-crown failure	None	Some	Some	Moderate	Moderate
		Surface VID	None	BV	BV	CV	CV

VID = Visible impact damage, BV = Barely visible, CV = Clearly visible

Table 5. Elastic constants and strength of E-Glass fibre and polymer matrix.

Properties	Material/Material property	TP matrix (Elium)		TS matrix (Epolam)		E-glass	
		Symbol	Value	Symbol	Value	Symbol	Value
Elastic constants	Modulus of Elasticity (GPa)	E_m [c]	3.10	E_m [b]	3.3	E_f [b]	73
	Modulus of Rigidity (GPa)	G_m	1.13	G_m	1.26	G_f [b]	30
	Poisson's Ratio	v_m [a]	0.37	v_m [d]	0.3	v_f [b]	0.22
Strength properties	Tensile strength (MPa)	T_m [c]	70	T_m [b]	65	T_f [d]	2000
	Compressive strength (MPa)	C_m [c]	130	C_m [d]	120	C_f [d]	1350
	Shear strength (MPa)	S_m	42	S_m	52		

[a] Reported in literature [14], [b] Reported in literature [30], [c] Reported in literature [29], [d] Reported in literature [53]

Table 6. The critical energy release rate of impregnated yarns in tension and compression along longitudinal (direction 1), in-plane transverse (direction 2) and out-of-plane transverse (direction 3) direction.

Critical energy release rate	G_{1c}^{1+} (N/mm)	G_{1c}^{1-} (N/mm)	$G_{2c}^{2+} = G_{3c}^{3+}$ (N/mm)	$G_{2c}^{2-} = G_{3c}^{3-}$ (N/mm)
E-Glass/Epoxy **[53]**	60	39.15	1.5	4
E-Glass/Elium	60	39.15	1.5	4

Table 7. Comparison of uniaxial results in thermoplastic and thermoset composites for tension and compression. The value in parenthesis represents an average of three samples.

Property/Material	Thermoplastic 3D composites			Thermoset 3D composites		
	Experiment	Simulation	% Difference	Experiment	Simulation	% Difference
Longitudinal tensile strength (MPa)	487 (±2.7)	507	3.9	461 (±16.5)	505	8.7
Transverse tensile strength (MPa)	465 (±4.5)	502	7.3	444 (±8.5)	495	10.3
Longitudinal comp. strength (MPa)	309 (±23)	369	16	272 (±20)	357	23
Transverse compressive strength (MPa)	362 (±5.2)	367	2.1	315 (±14)	355	11

Table 8. Comparison of computational time with other models

Studies compared	**Run time (min)**	**CPU cores**	**Element type**	**Contact properties**	**No of Ele.**
Turner et al. **[36]**	480	8	Shell element S4R	Penalty based contact Cohesive contact	210,000
Chu et al. **[37]**	900	32	Shell element S4R	Penalty based contact	-----
Current model	16	4	3D Solid Continuum C3D8R	Penalty based contact	3744

Figure 1

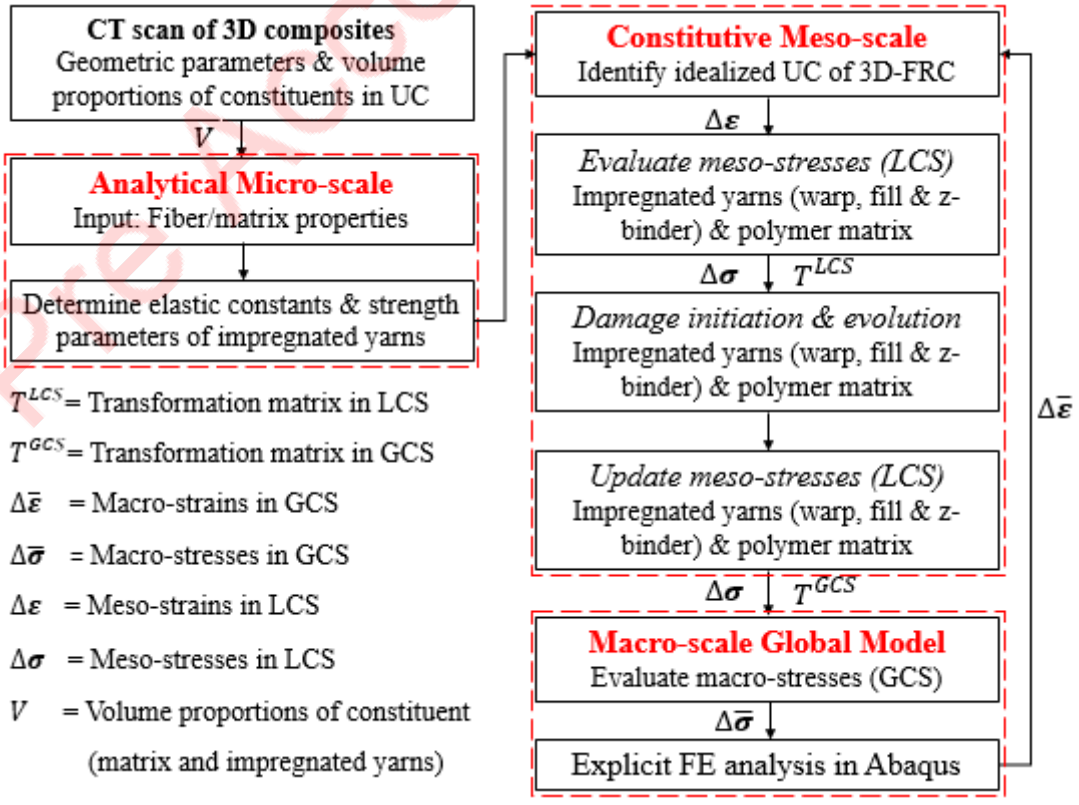

Figure 2

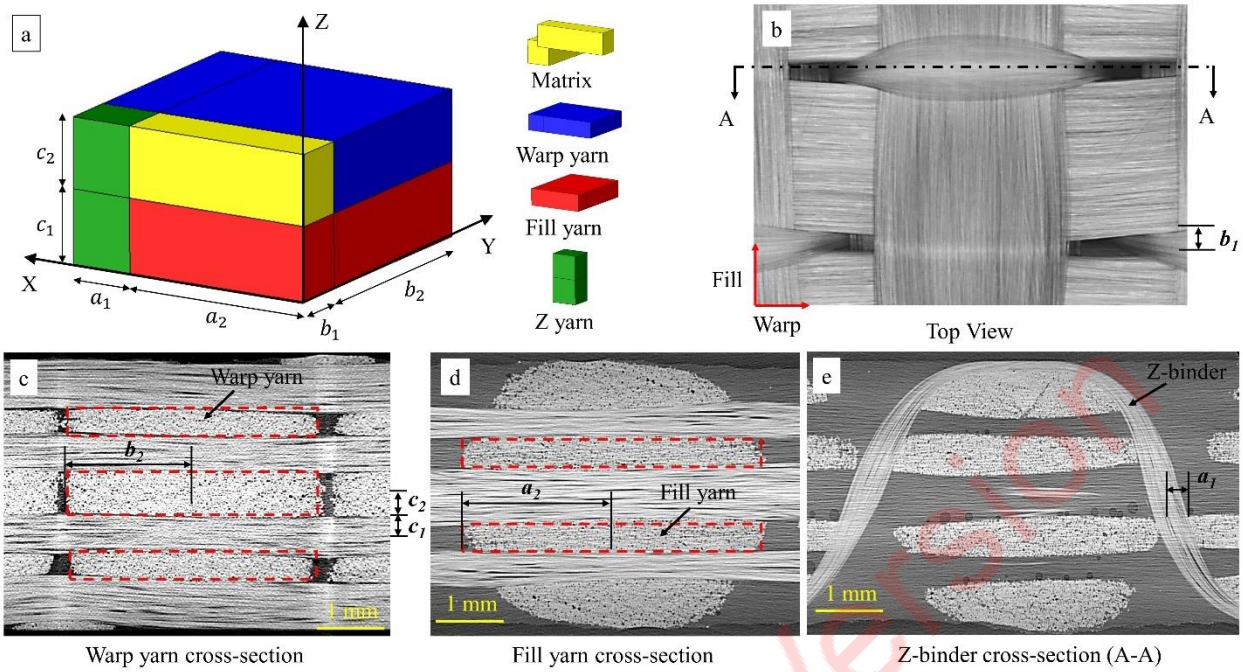

Figure 3

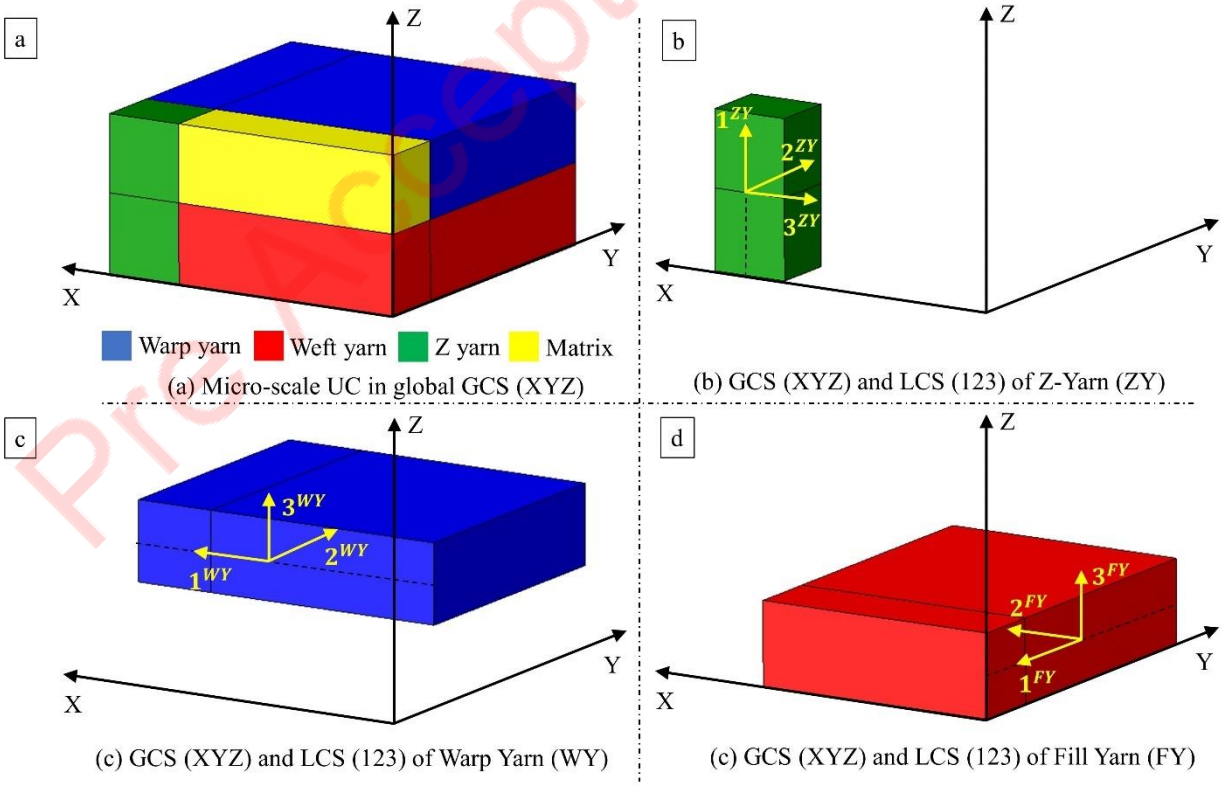

Figure 4

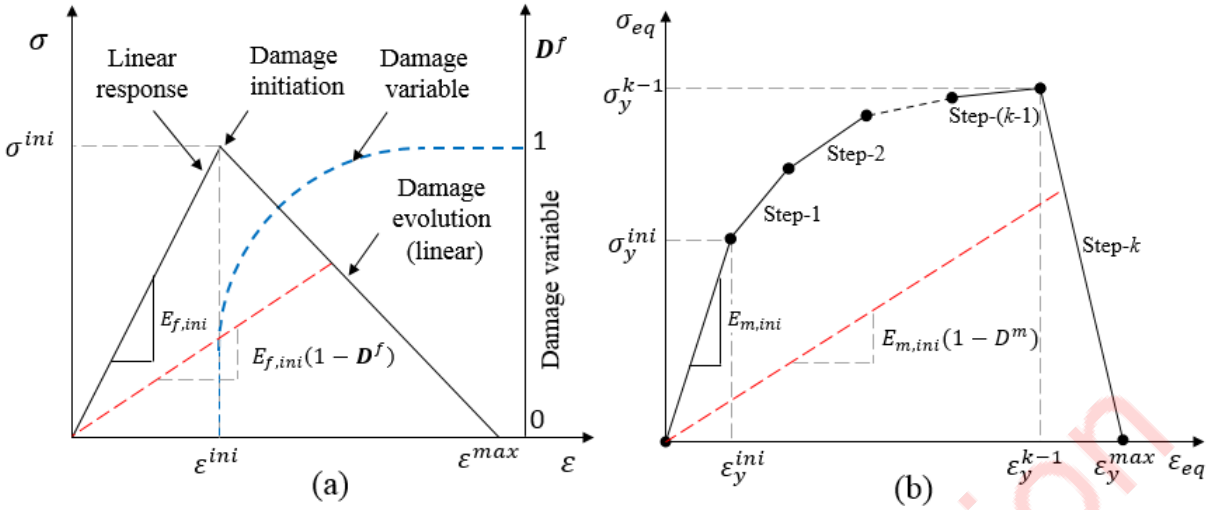

Figure 5

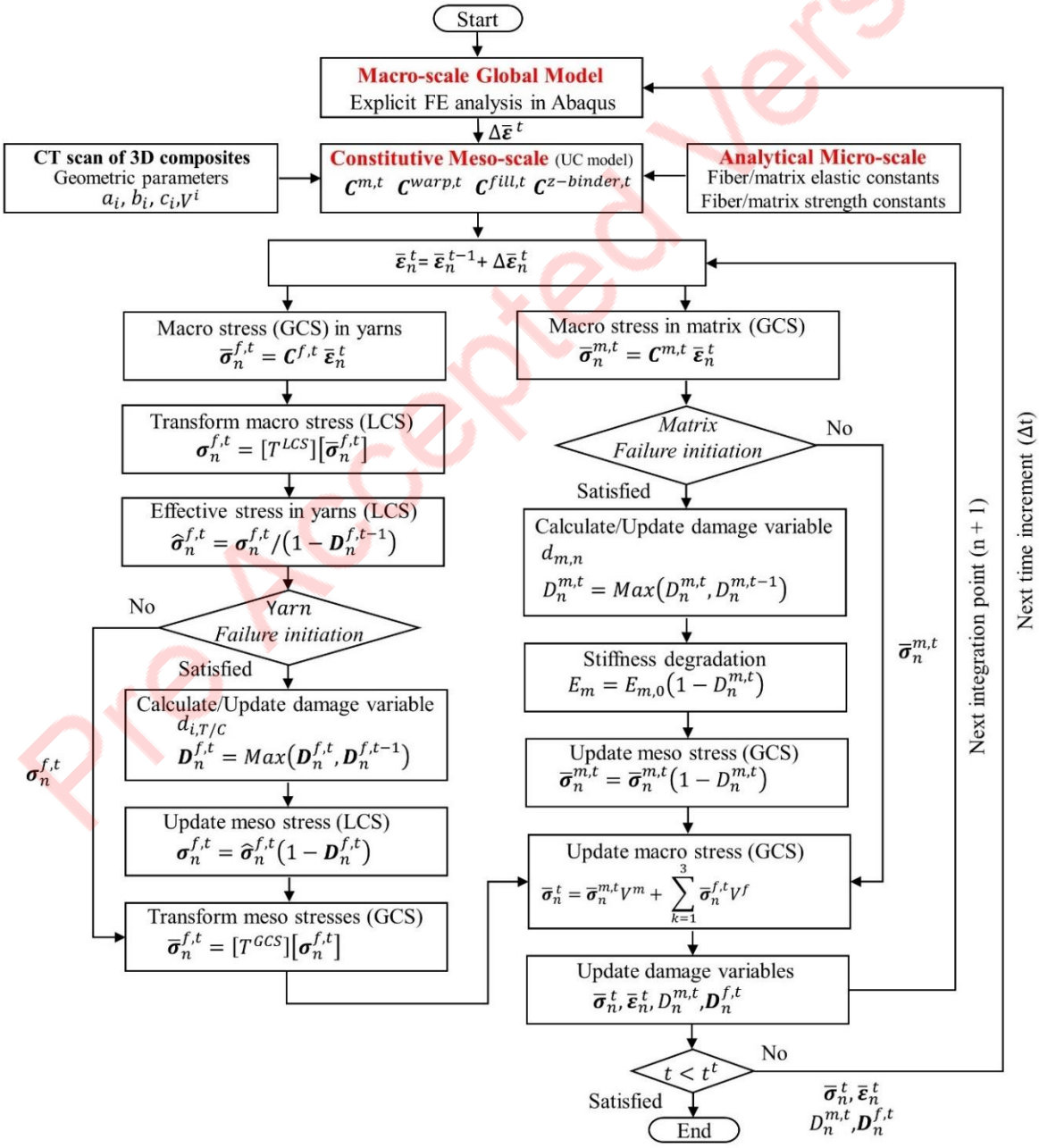

Figure 6

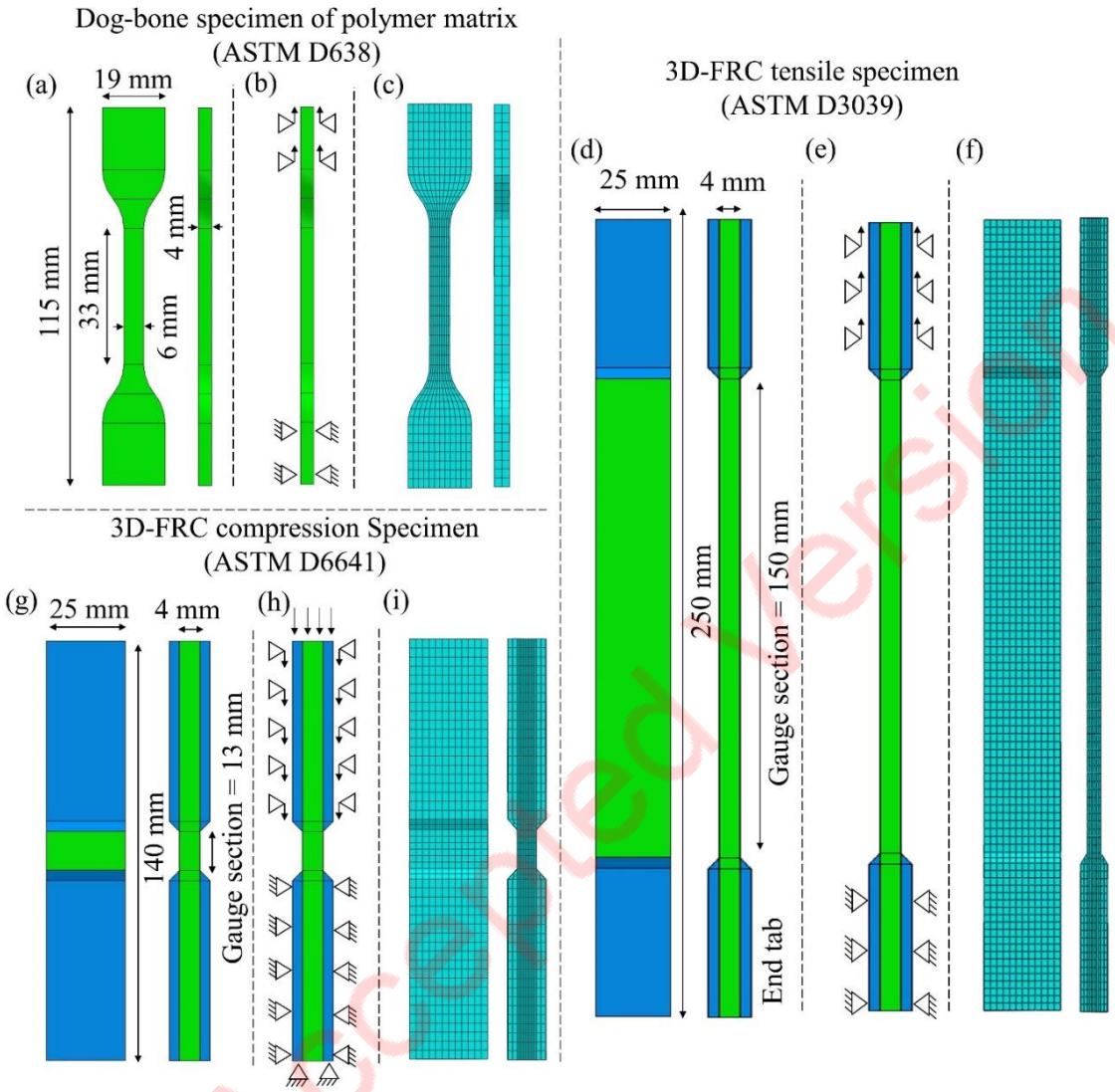

Figure 7

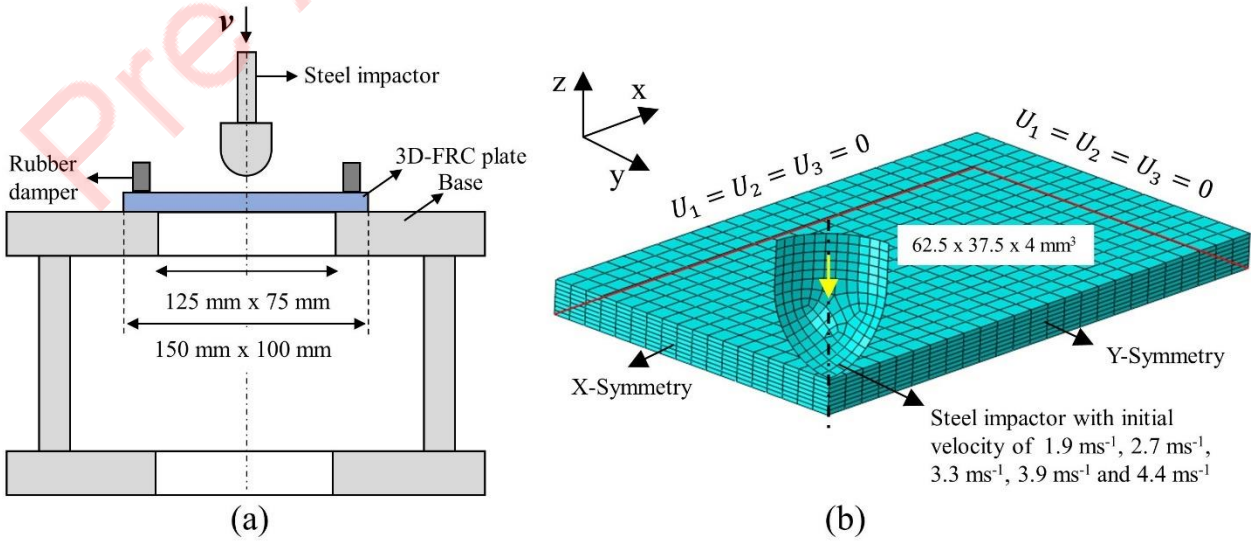

Figure 8

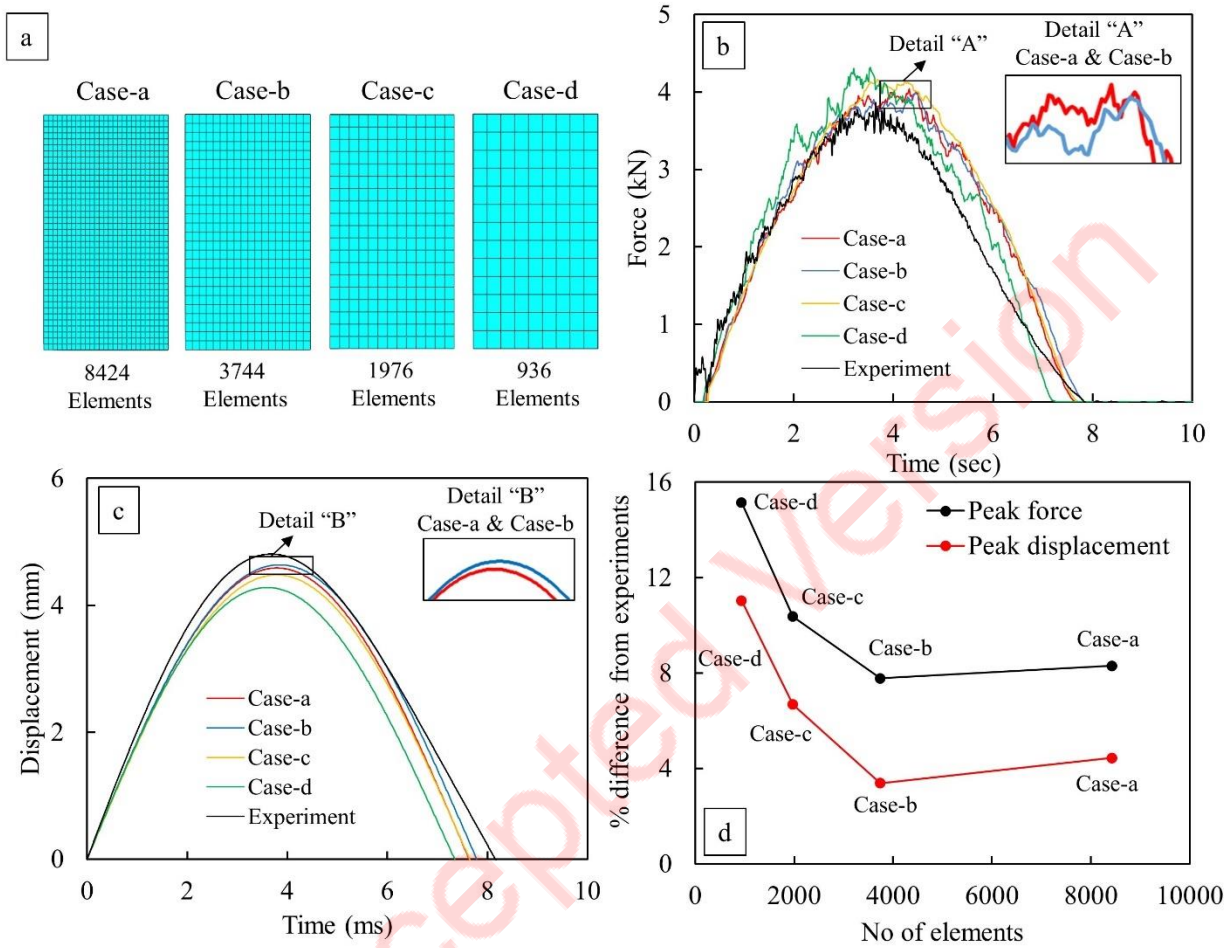

Figure 9

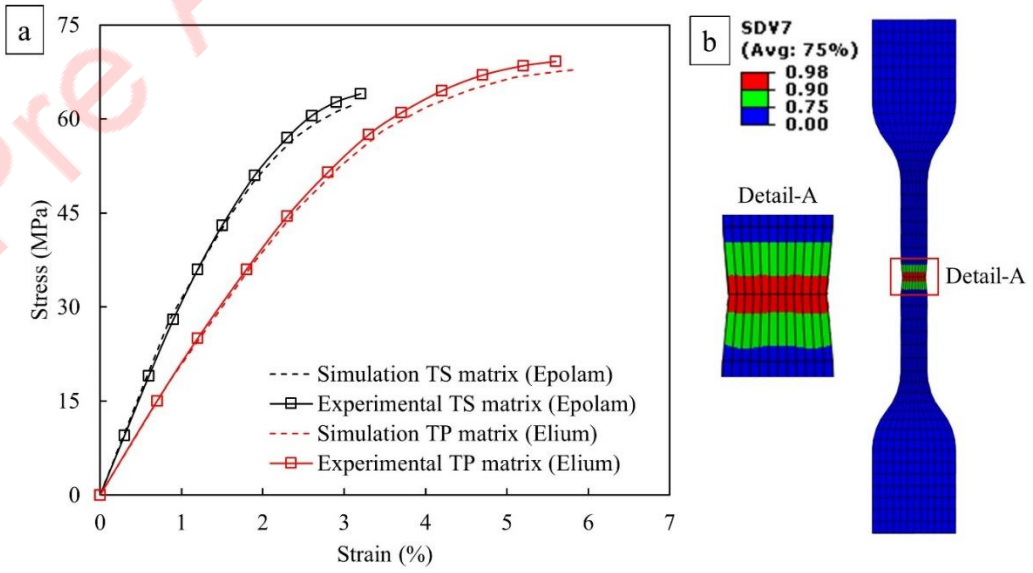

Figure 10

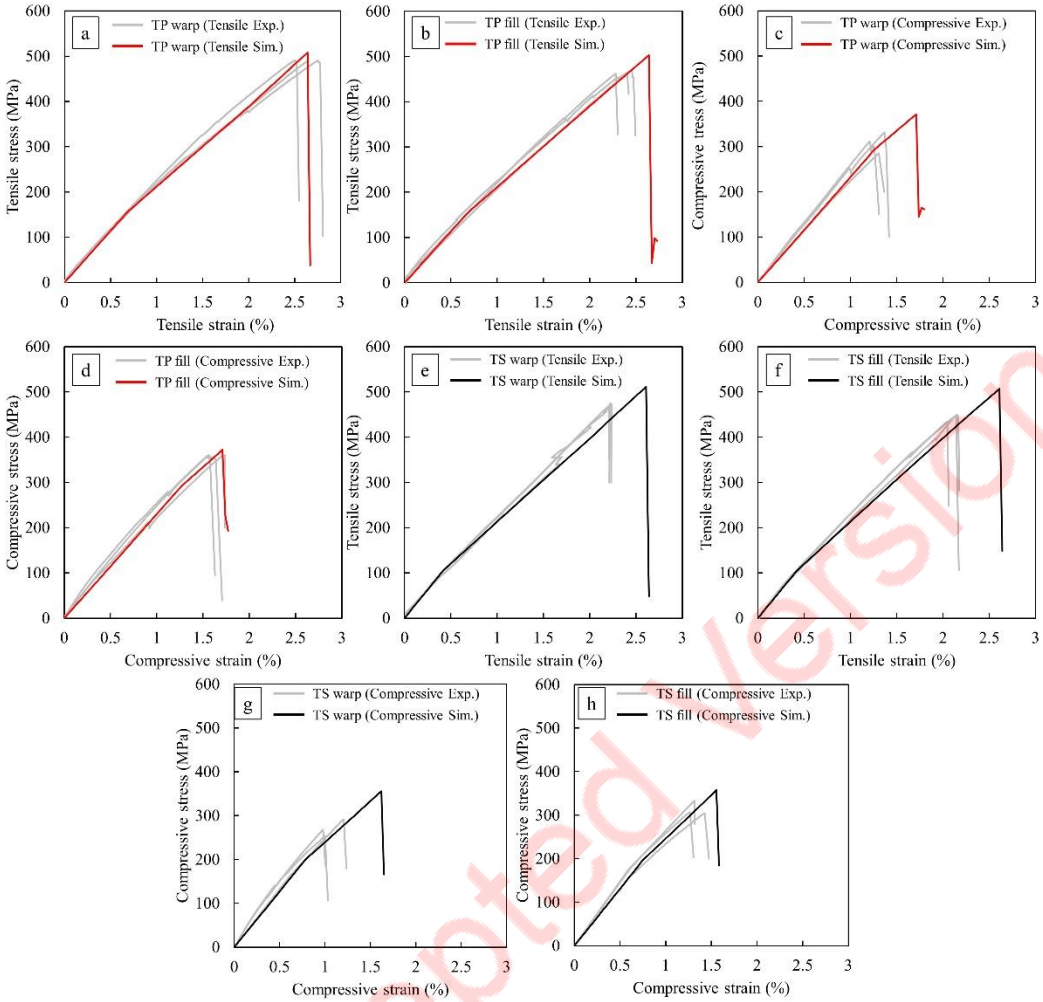

Figure 11

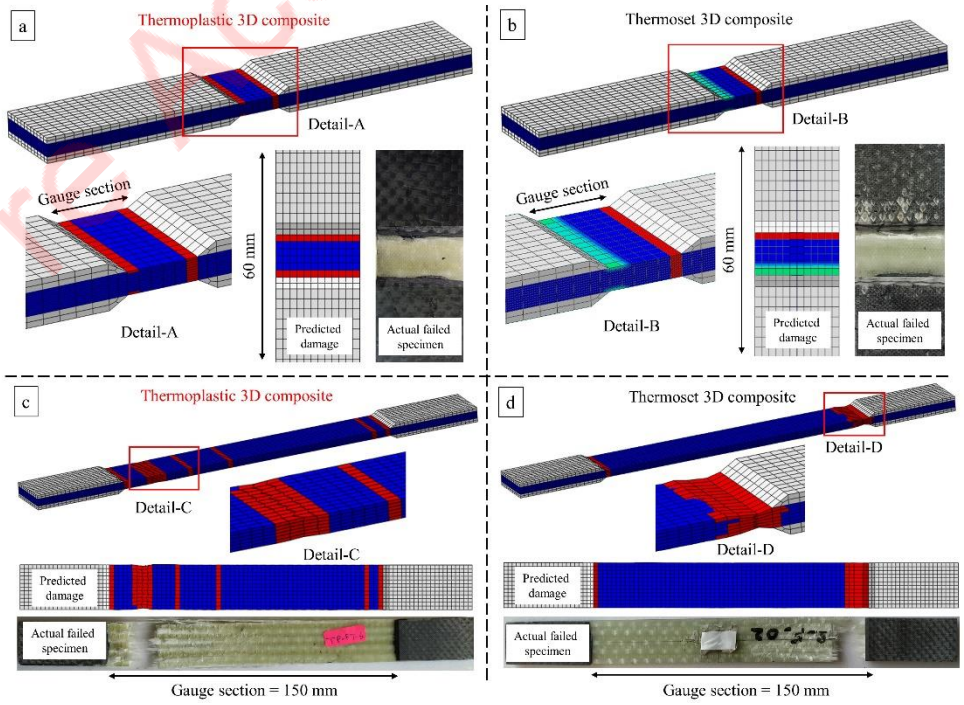

Figure 12

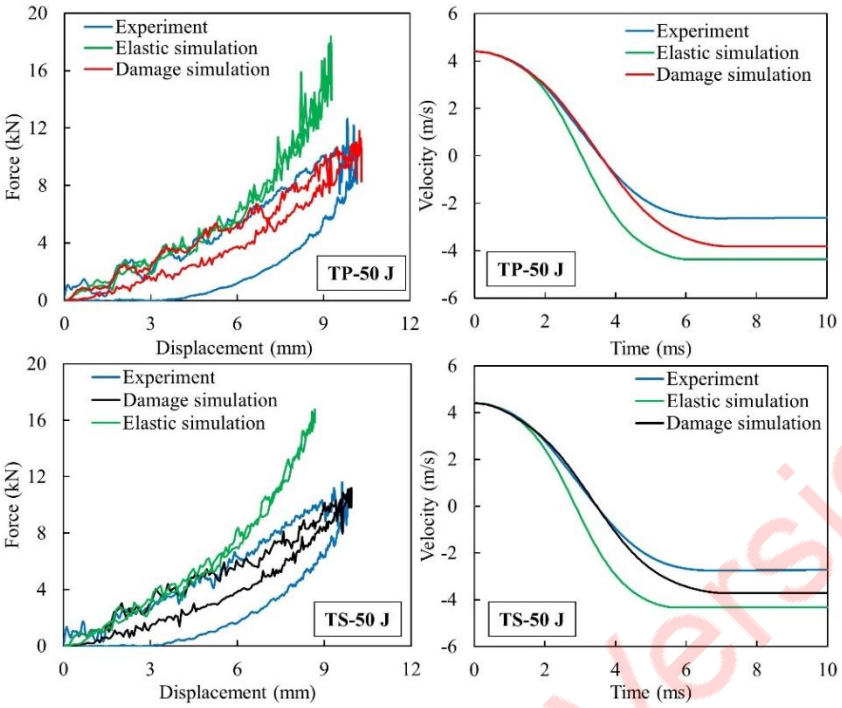

Figure 13

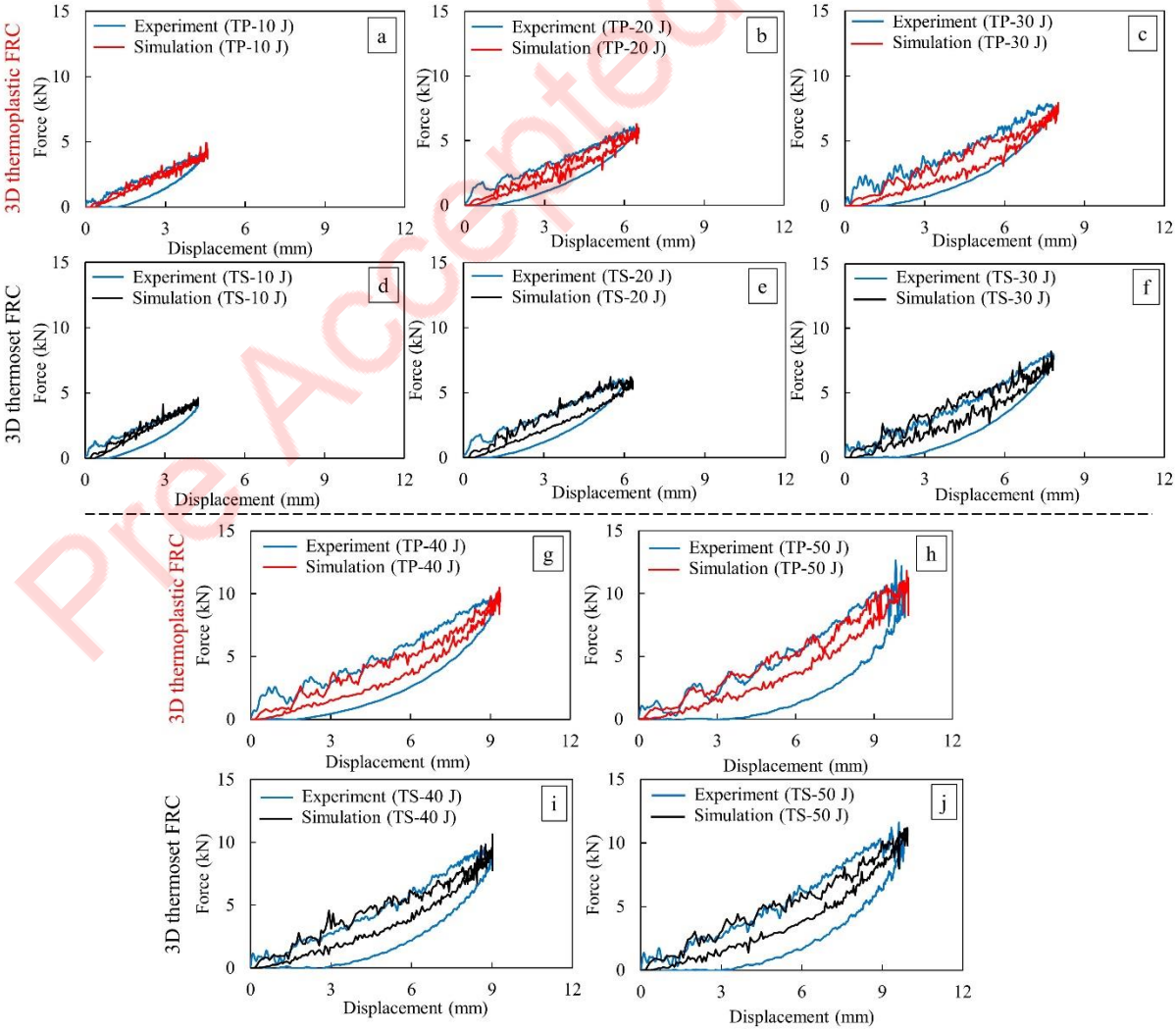

Figure 14

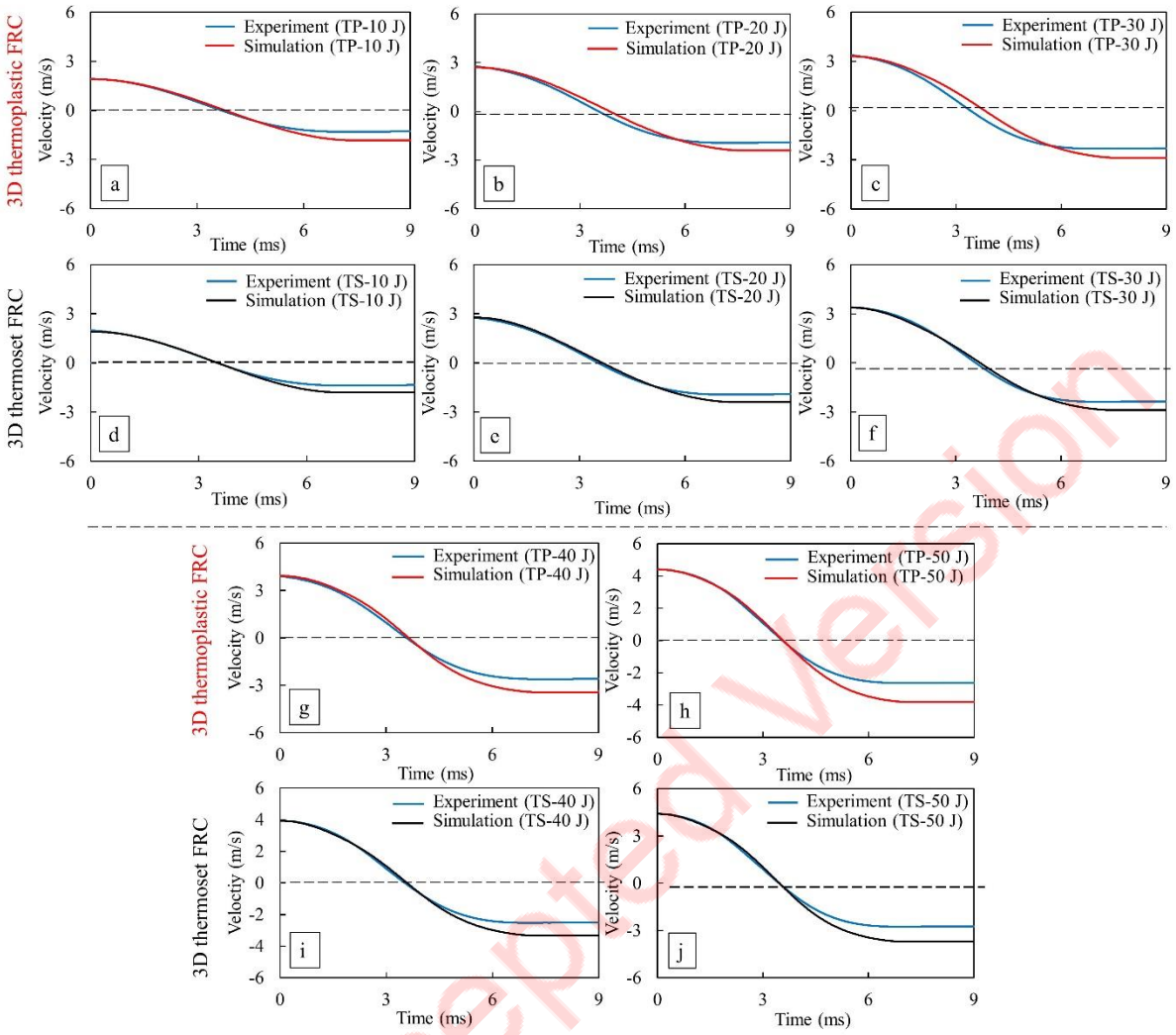

Figure 15

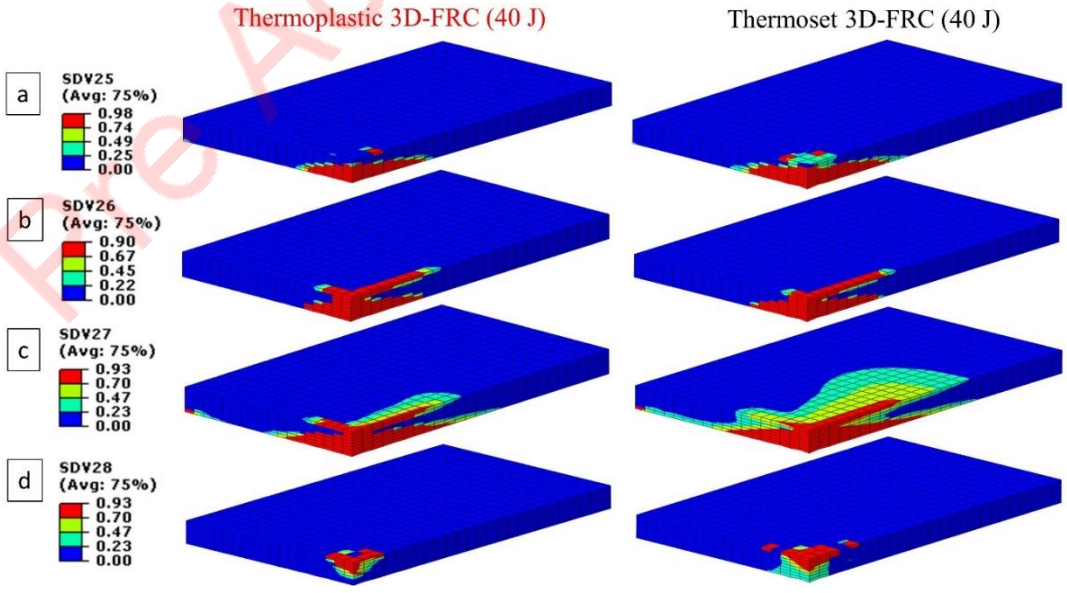

Figure 16